Astronomical forcing of meter-scale organic-rich mudstone–limestone cyclicity in the Eocene Dongying sag, China

Implications for shale reservoir exploration

Zhang, Jianguo; Jiang, Zaixing; Liang, Chao; Baars, Timothy F.; Wang, Youwei; Abels, Hemmo A.

DOI
10.1306/02072220103

Publication date
2022

Document Version
Final published version

Published in
AAPG Bulletin

Citation (APA)
Zhang, J., Jiang, Z., Liang, C., Baars, T. F., Wang, Y., & Abels, H. A. (2022). Astronomical forcing of meter-scale organic-rich mudstone–limestone cyclicity in the Eocene Dongying sag, China: Implications for shale reservoir exploration. *AAPG Bulletin*, *106*(8), 1557-1579. https://doi.org/10.1306/02072220103

Astronomical forcing of meter-scale organic-rich mudstone–limestone cyclicity in the Eocene Dongying sag, China: Implications for shale reservoir exploration

Jianguo Zhang, Zaixing Jiang, Chao Liang, Timothy F. Baars, Youwei Wang, and Hemmo A. Abels

ABSTRACT

The middle Eocene Dongying sag in the Bohai Bay Basin of China has an estimated shale oil resource of approximately 1.1 billion t (8.06 billion bbl); flows of shale oil have been produced in the succession from tens of wells, where the daily production of a single well generally varies between 10 and 100 t (73.3–733 bbl). Therein, the mudrock successions composed of meter-scale mudstone–limestone couplets are the most important shale oil-producing layers. The controls on the deposition of the meter-scale mudstone–limestone couplets, however, remain enigmatic, constraining the analysis of lithofacies and, therefore, sweet spot distributions. Here, we analyze three continuously cored organic-rich successions of mudstone–limestone couplets (371 m [1217 ft] in total) in the middle Eocene Dongying sag, accompanied by decimeter- to meter-scale sampling and testing of mineralogy, organic geochemistry, and paleontology of the rocks. Our integrated cyclostratigraphic analysis shows that the observed mudstone–limestone couplets occur at periods that coincide with Milankovitch periodicities; 21-k.y. precession cycles are the main driver of the meter-scale mudstone–limestone couplets, with additional imprints of 41-k.y. obliquity cycles. Specifically, precession minima are associated with high summer insolation and consequently high summer monsoonal precipitation, which increased river discharge and terrigenous input to the basin, resulting in the deposition of siliciclastic-rich mudstones. In the

Manuscript received June 24, 2020; provisional acceptance September 25, 2020; revised manuscript received May 26, 2021; revised manuscript provisional acceptance August 12, 2021; 2nd revised manuscript received August 29, 2021; final acceptance September 21, 2021.
DOI:10.1306/02072220103

AUTHORS

JIANGUO ZHANG ~ *School of Energy Resources, China University of Geosciences, Beijing, China; jianguozhangenergy@163.com, zhjianguo@cugb.edu.cn*

Jianguo Zhang is an associate professor at China University of Geosciences (Beijing). He received his Ph.D. from China University of Geosciences (Beijing) in 2017. His research focuses on mudrock sedimentology and shale reservoir prediction.

ZAIXING JIANG ~ *School of Energy Resources, China University of Geosciences, Beijing, China; jiangzx@cugb.edu.cn*

Zaixing Jiang is a professor of sedimentary geology at China University of Geosciences (Beijing). He received his Ph.D. from the Graduate School of Chinese Academy of Sciences in 1997. He is currently leading a group working on mudrock sedimentology.

CHAO LIANG ~ *School of Geosciences, China University of Petroleum (East China), Qingdao, China; State Key Laboratory of Shale Oil and Gas Enrichment Mechanisms and Effective Development, Sinopec Group, Beijing, China; liangchao0318@163.com; liangchao0318@upc.edu.cn*

Chao Liang is a professor at China University of Petroleum (East China). He received his Ph.D. from China University of Geosciences (Beijing) in 2015. His research focuses on mudrock sedimentology, sequence stratigraphy, mudrock diagenesis, and shale reservoir prediction.

TIMOTHY F. BAARS ~ *Department of Geosciences and Engineering, Delft University of Technology, Delft, the Netherlands; T.F.Baars@tudelft.nl*

Timothy F. Baars is a Ph.D. student of sedimentary geology at Delft University of Technology. His research focuses on improving the subsurface prediction of sedimentary systems based on stratigraphy and orbital forcing analysis.

YOUWEI WANG ~ *Department of Geosciences and Engineering, Delft University of Technology, Delft, the Netherlands; Youwei.Wang@tudelft.nl*

Youwei Wang is a Ph.D. student of sedimentary geology at Delft University of Technology. His research focuses on depositional response to upstream climate forcing through orbital forcing, outcrop analogue, and stratigraphic analysis.

HEMMO A. ABELS ~ *Department of Geosciences and Engineering, Delft University of Technology, Delft, the Netherlands; H.A.Abels@tudelft.nl*

Hemmo A. Abels is an assistant professor at Delft University of Technology. He received his Ph.D. at Utrecht University, the Netherlands, in 2008. His research focuses on implementation of models of astronomical climate forcing on stratigraphy into subsurface workflows.

ACKNOWLEDGMENTS

The study was cofunded by the National Natural Science Foundation of China (Grant nos. 41802130 and 41772090). We are grateful to the Analysis and Testing Center of the Geological Research Institute of Shengli Oil Company for permission to access the in-house database. We thank Delft University of Technology for hosting Jianguo Zhang during part of the study. We sincerely thank previous AAPG Editor Robert K. Merrill and three anonymous reviewers for their revisions and comments.

study, low summer insolation during precession maxima led to decreased summer monsoonal precipitation, lower river discharge and terrigenous input, and increased lake water salinity, resulting in the deposition of authigenic lime mudstones. The shale reservoir quality kept pace with the orbital climate changes; compared with lime mudstones deposited during precession maxima, mudstones deposited during precession minima had higher total organic carbon, porosity, and oil content, but lower brittleness.

INTRODUCTION

Meter-scale depositional cycles have been recorded in many basins worldwide, including the Carboniferous Paradox Basin, United States (Goldhammer et al., 1994); the Triassic Latemar Limestone, Italy (Hinnov and Goldhammer, 1991; Meyers, 2008); the Early Jurassic black shales, Bristol Channel Basin, United Kingdom (Hüsing et al., 2014; Xu et al., 2017); the Jurassic–Cretaceous Vaca Muerta Formation, Neuquén Basin, Argentina (Kietzmann et al., 2011, 2015); the Cretaceous black shale rhythms, central Italy (Herbert and Fischer, 1986; Tateo et al., 2000); the Cretaceous Western Interior of the United States (Kauffman et al., 1991; Sageman and Arthur, 1994; Ricken, 1996; Eldrett et al., 2015); the Paleogene pelagic sequence, northern Italy (Poletti et al., 2004); the Paleogene deep-marine Guaso System, Ainsa Basin, Spanish Pyrenees (Cantalejo and Pickering, 2014, 2015; Scotchman et al., 2015); and Quaternary deep-sea sediments, North Atlantic (Kominz, 1996). Several mechanisms have been introduced to explain the meter-scale lithofacies cycles, including control by orbital climate forcing changing sediment input, temperature, biogenic production, sea level (Goldhammer and Harris, 1989; D'Argenio et al., 1997; Pillans et al., 1998; Strasser et al., 2006; Kietzmann et al., 2015), local basin dynamics (Michalzik, 1996), and/or diagenetic redistribution of calcareous material (Westphal et al., 2000; Westphal and Munnecke, 2003; Su et al., 2020).

The widely distributed and thick (average 300–500 m [984–1640 ft]) organic-rich mudrock interval in the middle Eocene Dongying sag, eastern China, has an estimated shale oil resource of approximately 1.1 billion tons (8.06 billion barrels) (Ministry of Natural Resources, People's Republic of China, 2020). Shale oil flows of tens of tons to 100 t (hundreds to thousands of barrels) in daily production have been produced from dozens of wells from the sag over the last decade (Liang et al., 2017; Zhang et al., 2019a; Song et al., 2020), making it one of the most promising shale oil resource systems in China. The mudrock is composed of intervals with or without mudstone–limestone couplets. Therein, the intervals displaying meter-scale bedding of

mudstone–limestone couplets are the main producing layers. The differences in sedimentary structures, mineralogical composition, and arrangement along with lithofacies changes influence shale reservoir quality (Macquaker et al., 2014). However, controlling factors on lithofacies changes within the couplets are still unclear, constraining the analysis of shale reservoir distribution.

In this study, we demonstrate that the meter-scale lithofacies changes and the reservoir heterogeneity are predominantly triggered by Milankovitch climate changes. Precession cycles are the main driver of the meter-scale mudstone–limestone couplets associated with additional imprint by the obliquity cycles. This is based on analysis of approximately 371-m (~1217-ft) organic-rich mudrock successions from three continuously cored wells in the middle Eocene Dongying sag of eastern China, as well as decimeter-scale sampling and testing of mineralogy, total organic carbon (*TOC*), x-ray diffraction (XRD), spore and pollen, porosity, and Rock-Eval. The continuously cored mudrocks guarantee the accurate comparison of extracted orbital cycles and mudrock lithofacies changes.

GEOLOGICAL SETTING

Basin Filling

The Cenozoic Bohai Bay Basin, located in the eastern part of the Sino-Korean platform (Figure 1A), was formed by extensional to transtensional tectonics (Allen et al., 1997; Zhang et al., 2017). The Dongying sag is a lacustrine subbasin of the Bohai Bay Basin (Figure 1A). It was adjacent to the Chinese mainland to the west and the Pacific Ocean to the east during the middle Eocene (Figure 1A), covering an area of 6000 km^2 (Figure 1B). Proterozoic–Archaean granite, lower Paleozoic carbonate, and upper Paleozoic siliciclastic rocks of the North China craton are the main provenance rocks for the Cenozoic Dongying sag (Jiang, 2017), in which Eocene, Oligocene, Miocene, and Pliocene strata have been successively deposited (Figure 1C).

The target strata of this study are in the upper fourth member of the middle Eocene Shahejie Formation (Es_4^U) (Figure 1C), which is characterized by well-developed organic-rich mudrock (average 400 m [1312 ft] thick) in the lake center (Figure 1C). The water salinity varied between brackish to semisaline within our target layer, and its average water depth in the lake center is estimated to have been between 30 and 50 m (98–164 ft) (Li et al., 2003; Zhang et al., 2021).

Climate Setting

During the middle Eocene, the Dongying sag was located at approximately 119°E and 37°N, and warmer and more humid climates alternated with colder and drier climates (Lei et al., 2018). In general, the mean annual temperature (MAT) was between 16°C and 19°C (60.8°F–66.2°F), and the mean annual precipitation was 1100–1300 mm during the deposition of Es_4^U (Jiang et al., 2007).

The Eocene East Asian climate has long been known to be controlled by the planetary wind system. This monsoonal system includes both winter and summer monsoonal circulation (Figure 1A). During winter seasons, cold and dry Siberian air over continental regions and warm air over the Pacific Ocean produced a strong land–sea pressure gradient that forced cold and dry northeasterly winds to flow over East Asia (Figure 1A). During summer seasons, dominant wind directions reversed due to reversed pressure gradients, and moisture-bearing summer winds swept over the East Asian continent, reaching as far as the northern part of China (Figure 1A), causing increased summer rainfall. Recently, intensified monsoonal or monsoon-like middle Eocene climates have been broadly reported in the northern, middle, and southern East Asia (Licht et al., 2014; Quan et al., 2014; Ma et al., 2019).

DATA AND METHODS

Sedimentology, Paleontology, and Reservoir Analysis

The data are based on well logs and core samples from the wells Fanye1, Liye1, and Niuye1 (Figure 1B). The cores are continuous and have thicknesses of 131 m (430 ft), Fanye1; 110 m (361 ft), Niuye1; and 130 m (427 ft), Liye1. All of the cores are vertically cut along the diameter of the cylinder and then continuously photographed by the core-scanning

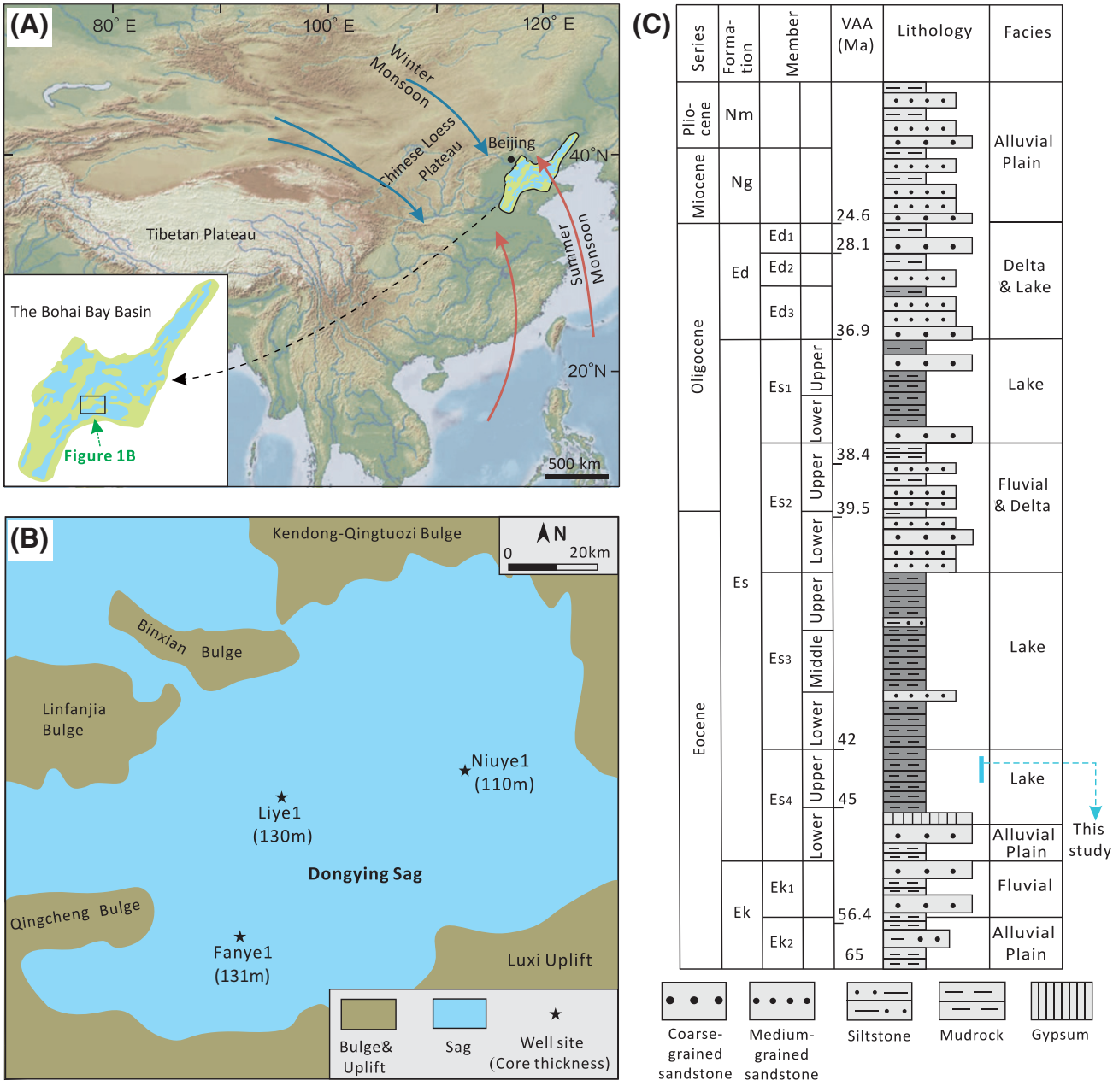

Figure 1. (A) Location of the Bohai Bay Basin in East Asia. The red and blue arrows indicate the direction of the middle Eocene summer and winter monsoons, respectively (monsoon directions adapted from Licht et al., 2014). The black rectangle (inset) in the Bohai Bay Basin shows the location of the Dongying sag. (B) Locations of cored wells in this study (annotated by stars). Core thicknesses of this study are annotated in the parentheses. (C) Cenozoic stratigraphy of the Dongying sag. The target strata of this study are annotated with a blue line. The volcanic ash age (VAA) is adapted from Yao et al. (2007a, b). In the lithology column, the dark-gray mudrock represents deep-water environment, while light-gray mudrock represents shallow-water environment. Ed = Eocene Dongying Formation; Ek = Eocene Kongdian Formation; Es = Eocene Shahejie Formation; Ng = Neogene Guantao Formation; Nm = Neogene Minghuazhen Formation.

equipment. The sampling intervals for the analyses of *TOC* and XRD are 1–2 m (3.3–6.6 ft) and approximately 0.5 m (1.6 ft) in Fanye1, approximately 1 m (3.3 ft) and 0.25 m (0.82 ft) in Niuye1, and 1–5 m (3.3–16.5 ft) and 1–4 m (3.3–13.2 ft) in Liye1. The sampling intervals of porosity and Rock-Eval are 1–2 m (3.3–6.6 ft) in all three wells. Spore and pollen analyses have been conducted on 3334–3436 m (10,938–11,272 ft) of the Niuye1 core, at a sampling interval of 0.5–1 m (1.6–3.3 ft). Methods for testing *TOC*, XRD, porosity, Rock-Eval, and spore and pollen data are described by Zhang et al. (2016a, b).

Grain-size analysis was conducted on samples of the three wells by thin-section photography. Digital photographs of thin sections were taken using a Zeiss Axio microscope (Scope A1), and then the identifiable quartz particles were marked and measured. Grain sizes of more than 100 particles were measured in each thin section using USFEN L1 software.

Cyclostratigraphic Analysis

The cyclostratigraphic analysis was based on the high-resolution natural gamma-ray (GR) logging data that were acquired downhole over the entire cored intervals of the three wells at a spacing of 0.1 m (0.3 ft). Low GR values of 55 to 70 API were found to coincide with the occurrence of lime mudstones, whereas high GR values of 70 to 95 API generally corresponded to mudstones. As shown in this paper, the observed cyclicity and high resolution of the GR curve suggest that the data satisfied the requirements for Milankovitch cycle analysis. The spectrum analysis was then conducted to detect the traces of Milankovitch cycles in mudrocks.

Before spectral analysis, we created an average stratigraphy by bed-to-bed correlation of the three wells. This was achieved by correlating the three wells based on visual peak matching of high GR values. Assuming that each peak represented one cycle boundary, the new cycle thickness was calculated by the mean cycle thickness of the three wells. The cumulative sum of the new cycle thickness was used to form a new averaged depth scale. The wells were then transposed on this new depth scale using the AnalySeries 1.1 program of Paillard et al. (1996). Afterward, the GR values of the transposed wells were normalized and the mean was taken to form an average GR curve on which spectral analysis can be applied.

Spectral analysis was applied to the data using the REDFIT program (a Fortran 90 program) (Schulz and Mudelsee, 2002). Time-series analyses of GR data were performed first using the REDFIT program (Schulz and Mudelsee, 2002) with a rectangular window and standard settings and then by the AnalySeries 1.1 program of Paillard et al. (1996) using the Blackman-Tukey method by having a Bartlett window. Bandpass filtering was subsequently performed using the AnalySeries program.

RESULTS

The detailed sedimentological, spore and pollen, reservoir, and cyclostratigraphic characteristics of the mudrock are described and summarized in Table 1.

Sedimentary Characteristics

Quartz, feldspar, clay, and calcite account for more than 95 wt. % of all of the minerals in the studied interval (Table 1). The mudrock is composed of mudstones containing more than 50% siliciclastics (quartz + feldspar + clay) and lime mudstones containing more than 50 wt. % calcite (Figure 2). Specifically, the content of calcite is found to be negatively correlated with quartz (Figure 3A) and clay (Figure 3B). Since the content of *TOC* shows a positive correlation with quartz (Figure 3C), the content of calcite is also adversely related to that of *TOC* (Figure 3D). A mudstone–limestone cycle is typically 2 to 3 m (6.6 to 9.8 ft) thick and has both sharp and gradual interfaces between mudstones and lime mudstones (Figure 4). Both mudstones and lime mudstones are laterally traceable over distances of up to 73 km (45.4 mi) (Figure 5).

Mudstones

Description—Dominantly dark to black mudstones account for one-quarter to one-third of the total thickness of a mudstone–limestone cycle (Figure 4). The mudstones are mainly composed of quartz (average 28 wt. %), clay (average 31 wt. %), calcite (average 19 wt. %), feldspar (average 9 wt. %), and dolomite (average 8 wt. %) (Table 1). The *TOC* content varies between 2.5 and 12 wt. % (average 4.9 wt. %), suggesting high organic matter abundance.

The mudstones are very finely laminated, generally of alternating siliciclastic- and clay-rich lamina. The siliciclastic-rich laminae are 100–500 μm thick (Figure 6A–D) and consist dominantly of quartz, and clay "particles" as well as organic matter. The quartz particles are 10–30 μm in size and angular to subangular in shape (Figure 6A–D), and almost all are purple or brown under the cathode luminescence (see figure 4D in Zhang, 2017), suggesting a terrigenous origin. The particle size shows a weak fining-upward trend through the laminae (Figure 6C, D).

The clay-rich laminae have a thickness of 50 to 250 μm (Figure 6A–D); quartz particles episodically

Table 1. Overall Sedimentology, Well Log, Paleontology, and Cyclostratigraphic Characteristics of the Mudrock of the Middle Eocene Shahejie Formation

Proxies	Mudstone	Lime mudstone	Interpretation
Sedimentology (Figures 2–7)			
Minerals	Calcite = 6–28 wt. % (avg. 19 wt. %) Dolomite = 3–15 wt. % (avg. 8 wt. %) Quartz = 16–39 wt. % (avg. 28 wt. %) Feldspar = 2–14 wt. % (avg. 9 wt. %) Clay = 18–40 wt. % (avg. 31 wt. %)	Calcite = 36–62 wt. % (avg. 51 wt. %) Dolomite = 2–17 wt. % (avg. 9 wt. %) Quartz = 6–22 wt. % (avg. 11 wt. %) Feldspar = 1–6 wt. % (avg. 3 wt. %) Clay = 14–29 wt. % (avg. 23 wt. %)	Higher clastic mineral content for mudstones
Structures			
Laminae	Alternating clastic laminae and clay laminae	Alternating lime mud laminae and clay laminae	Higher terrigenous input for mudstones
Fining-upward sequence	+	–	Clastic mudstone deposited by suspension setting
Evaporitic minerals	–	+	More saline water for lime mudstones
Organic matter			
Type	Dominated by type I, with some type II		Authigenic organisms are dominant in both lithofacies
Content (wt. %)	2.5–12 (avg. 4.9)	1.2–5.1 (avg. 2)	Higher *TOC* content for mudstones
Well log (Figure 8)			
GR	70–95 API	55–70 API	Higher radioactivity and clay input for mudstones
Spore and pollen (Figure 8)	*HI* = 0.5–1 (avg. 0.8), *TI* = 0.4–0.8 (avg. 0.69)	*HI* = 0.33–0.5 (avg. 0.46), *TI* = 0.2–0.4 (avg. 0.29)	More humid and warm climate for mudstones
Shale reservoir property (Figures 9, 10)			
Porosity (%)	8.5–17.8 (avg. 12.3)	6.3–12.1 (avg. 9.2)	Higher porosity for mudstones
S_1 (mg/g)	3.9–11.3 (avg. 7.1)	2.3–5.8 (avg. 3.9)	Higher oil content for mudstones
Brittleness index	0.52–0.79 (avg. 0.64)	0.56–0.93 (avg. 0.74)	Higher brittleness index for lime mudstones
Cyclostratigraphic interpretation (Figures 10–12)	Precession minimum	Precession maximum	Increased runoff and temperatures during high summer insolation that corresponds to precession minima

Abbreviations: + = common in the rock; – = sparse in the rock; avg. = average; GR = gamma ray; *HI* = humidity index; S_1 = the amount of free hydrocarbons in Rock-Eval pyrolysis analysis; *TI* = temperature index; *TOC* = total organic carbon.

occur parallel to bedding, are generally of coarser grain sizes (mostly 4–6 φ [15.6–62.5 μm]) than the other minerals (Figure 6E), and show a weak negative skewness (Figure 6F). Organic matter is also widely seen in this type of laminae (Figure 6A–D), whereas no fining-upward or coarsening-upward characteristics are observed.

Both types of laminae are laterally consistent in thickness at the core scale (9 cm [3.5 in.] wide).

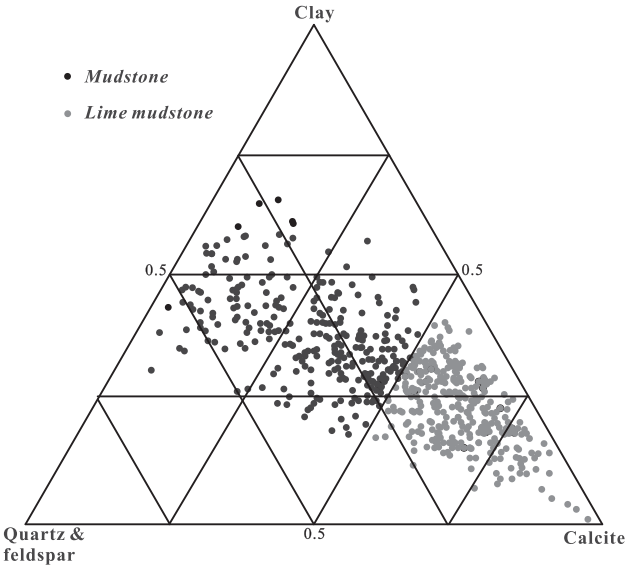

Figure 2. Ternary diagram illustrating the mineralogical composition of mudrock in the fourth member of the middle Eocene Shahejie Formation. "Lime mudstone" refers to samples with a calcite content >50 wt. %, whereas "mudstone" refers to samples with a calcite content <50 wt. % (quartz + feldspar + clay >50 wt. %).

Interpretation—The regularly alternating siliciclastic-rich and clay-dominant laminae are believed to be siliciclastic varves that have formed under high terrigenous input conditions. Specifically, three depositional mechanisms have been established to explain the formation of siliciclastic-rich laminae in basins worldwide: (1) distal turbidites (Schieber, 2016; Yang et al., 2017a, b); (2) dust storms (Potter et al., 2005); and (3) suspension settling in high terrigenous input environments (Zhang and Sha, 2012; Schimmelmann et al., 2016; Tylmann and Zolitschka, 2020). However, a turbiditic origin can hardly explain the laterally constant thickness of laminae in cores and thin sections (Figures 4; 6A, B) (Potter et al., 2005; Plint et al., 2012), and dust storms seldom transport organic matter and clay (Bishop et al., 2002). Therefore, these siliciclastic laminae are interpreted to have formed by suspension settling in a high terrigenous input environment (Lapointe et al., 2012; Ridge et al., 2012).

During the middle Eocene, cold winter in combination with overall warmer climate throughout the

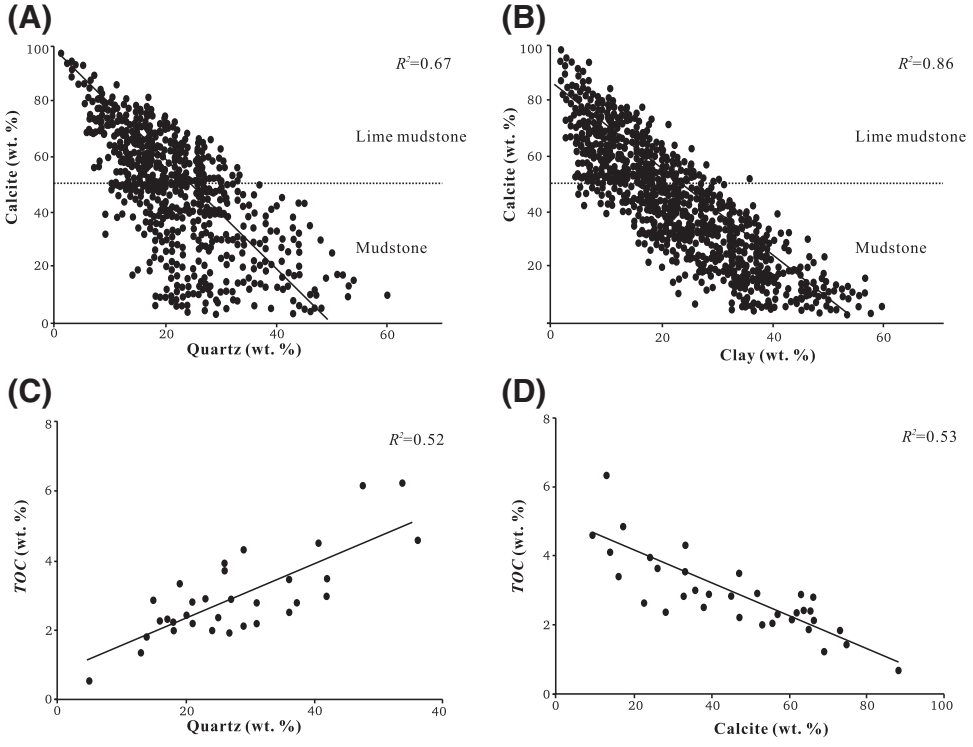

Figure 3. Crossplots showing the relationship of calcite, quartz, clay, and total organic carbon (*TOC*) in the middle Eocene Shahejie Formation. (A) Negative relationship between calcite and quartz. (B) Negative correlation between calcite and clay. (C) Positive relationship between *TOC* and quartz. (D) Negative relationship between *TOC* and calcite. Since the content of *TOC* is positively correlated with that of terrigenous minerals and negatively correlated with that of authigenic calcite, the corresponding organic matter may be enriched as a result of an environment having high terrigenous input. R^2 = coefficient of determination.

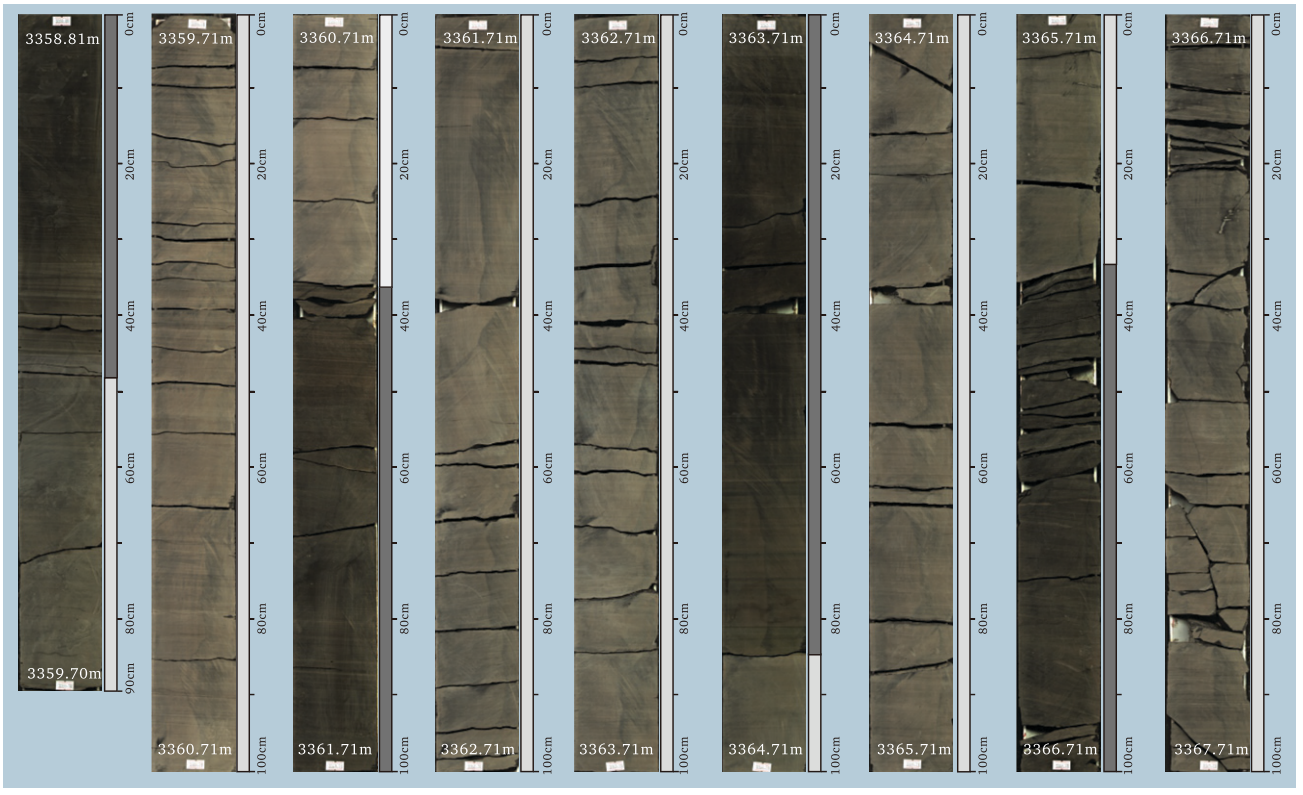

Figure 4. Photographs of 9 m (29.5 ft) of cored mudrock of the middle Eocene Shahejie Formation in well Niuye1. The series is composed of alternating mudstones (dark rocks along with gray bars to the right) and lime mudstones (pale-gray rocks with light-gray bars to the right). The lithofacies transition from lime mudstones to mudstones is gradual at 3359.2 m (11,021.0 ft) and sharp in the other interfaces. Diagonal and horizontal cracks result from the pressure relief after core collection.

rest of the year resulted in the snow melting in the early spring (Jiang, 2017). In this context, relatively high-density minerals (e.g., quartz, feldspar, large-size clay floccules) were carried and deposited in spring to summer, forming siliciclastic-rich laminae (Figure 6A, B). Only clay "particles" were carried by rivers during cold seasons because turbulent flows were more inhibited in a cold season than in a warm season due to the significantly reduced water runoff, forming very-fine-grained clay-dominant laminae. Therefore, the siliciclastic-rich and clay-rich laminae sets were interpreted to represent varve deposits.

Quartz particles in the clay-dominant laminae are well sorted and their grain sizes are mostly concentrated in the range of 4 to 6 φ (15.6–62.5 μm) (Figure 6F). The grain size distribution and curve morphology pattern of these quartz particles share high similarity with those of the deposits in the Chinese loess plateau (Figure 6F; Lu and An, 1999; Wang, 2007). The high similarity between quartz particles in the study area and those in the northwestern Chinese loess plateau in terms of grain size distribution features suggest their similar source. Moreover, the wind-driven quartz particles that originate from the Chinese loess plateau have been demonstrated to be present in the Eocene deposits in the Bohai Bay Basin (Wang, 2007) and the Xining Basin (Licht et al., 2014) of East Asia in previous studies, suggesting that these quartz particles could be loess deposits.

Lime Mudstones

Description—Lime mudstones are pale to pale gray in color and account for two-thirds to three-quarters of the total thickness in a mudstone–limestone cycle (Figure 4). They are mainly composed of calcite (average 51 wt. %), feldspar (average 3 wt. %), dolomite (average 9 wt. %), quartz (average 11 wt. %), clay (average 23 wt. %) (Table 1), and a small amount of secondary halite and anhydrite (1–3 wt. %) in approximately 10% of the lime mudstone intervals. The *TOC* content varies between 1.2 and 5.1 wt. %

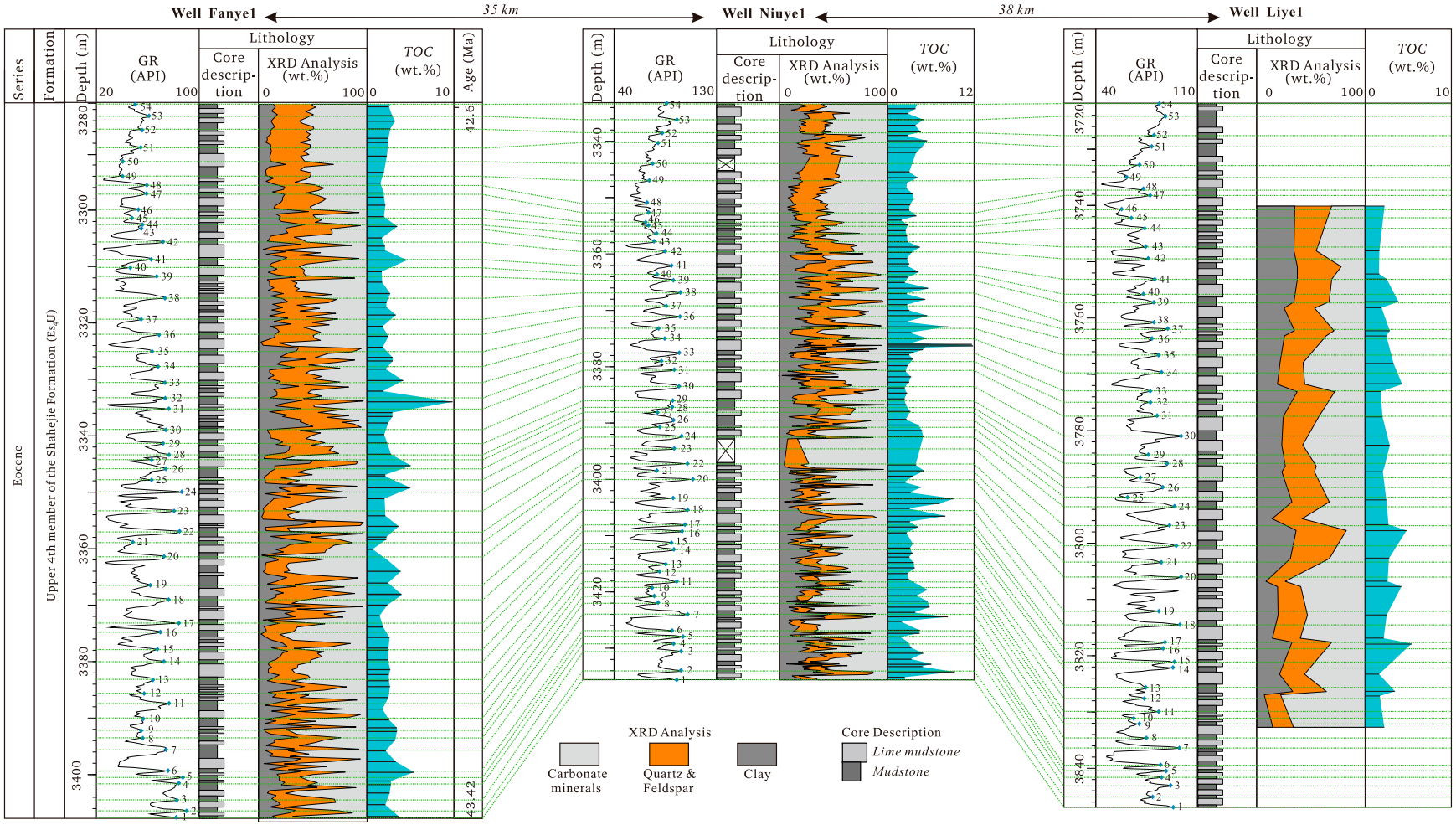

Figure 5. Variations of gamma ray (GR), lithology, x-ray diffraction (XRD), and total organic carbon (*TOC*) with burial depths for the Es_4^U in wells Fanye1, Niuye1, and Liye1. The sampling resolution varies in three wells (see the Data and Methods section). The lithology columns for wells Fanye1, Niuye1, and Liye1 are drawn according to the mineral composition data and core image observation. A total of 53 cycles are found to be commonly present in the GR logs of all three wells, with the peaks successively numbered from 1 to 54. Peaks having high GR values are artificially set as the cycle boundary. The 53 cycles have a wide thickness range of 0.7–6 m (average 2.33 m) (2.3–19.7 ft [average 7.64 ft]), with a standard deviation of 0.4 m (1.3 ft). The core depth correction was conducted through one-to-one comparisons between GR cycles and core lithofacies cycles, in which the well logs are found to be 0.9 m (2.95 ft) deeper in Fanye1, 0.6 m (1.97 ft) deeper in Niuye1, and 1.2 m (3.94 ft) deeper in Liye1 than core depth.

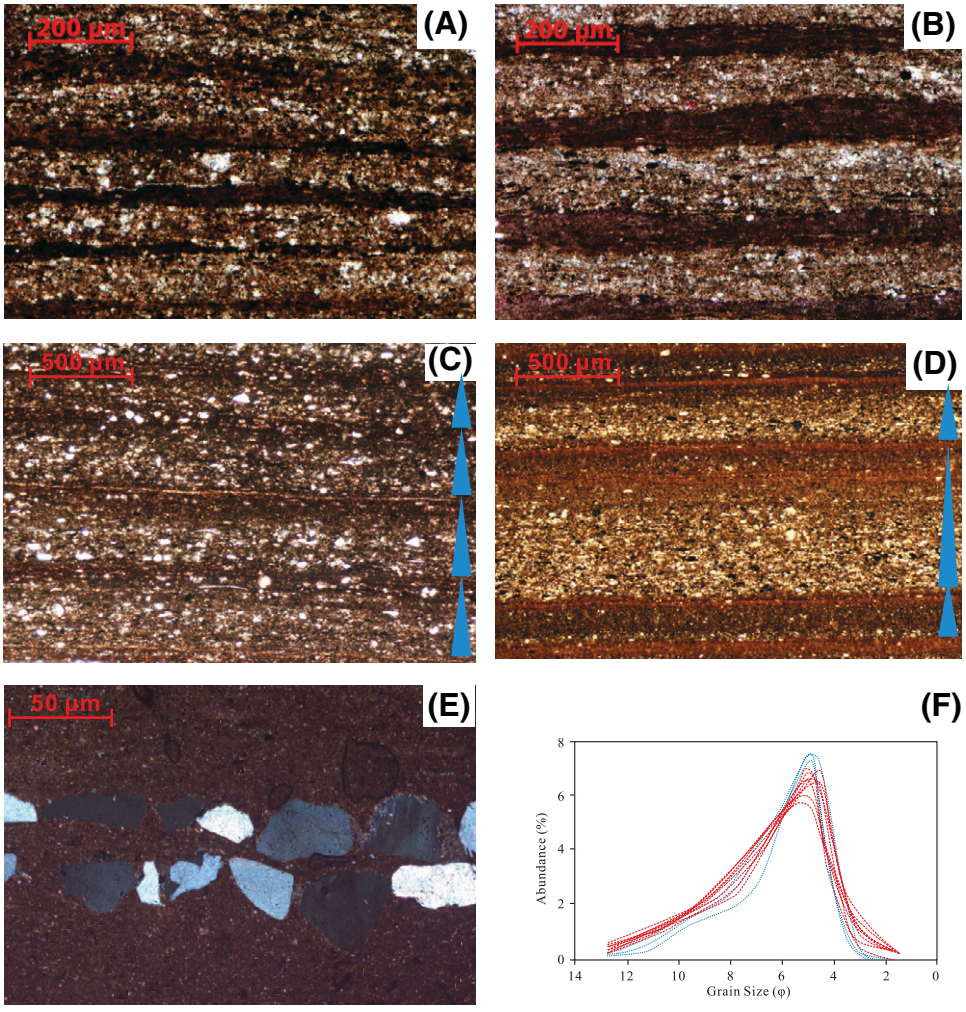

Figure 6. Petrological characteristics of mudstones of the middle Eocene Shahejie Formation in well Niuye1. See Figure 1B for the well location and Figure 8 for the stratigraphic locations of these photographs in the well. (A) Vertically alternating silciclastic-rich and clay-rich laminae having laterally consistent thicknesses, 3358.95 m (11,020.18 ft). (B) Vertically alternating siliciclastic-rich and clay-rich laminae, 3361.60 m (11,028.87 ft). (C) Weakly fining-upward sequence (blue arrowheads) illustrating the transition from siliciclastic-rich laminae to clay-rich laminae, 3366.35 m (11,044.46 ft). (D) Weakly fining-upward sequence (blue arrowheads) from the siliciclastic-rich laminae to clay-rich laminae, 3364.23 m (11,037.50 ft). (E) Laterally distributed quartz particles (30–60 μm) in clay-rich laminae, 3366.10 m (11,043.64 ft). (F) Comparison of a selection of grain-size distributions of mudstone samples in this study (red dotted lines) with those of the samples from the Chinese Loess plateau (blue dotted lines) of Lu and An (1999).

(average 2 wt. %), which is lower than that in the mudstone interlayers.

These lime mudstones are mostly laminated and consist of lime mud laminae (100–500 μm thick) and clay-dominant laminae (20–100 μm thick) (Figure 7A, B). Quartz and feldspar are rarely observed in the lime mud laminae (Figure 7A, B). Both types of laminae are laterally consistent in thickness at the core scale (9 cm [3.5 in.] wide) and do not have any fining- or coarsening-upward characteristics. Some lime mud laminae are bioturbated, and the corresponding lime mud "particles" occur in the forms of lenticular (Figure 7C) or mottled aggregates (Figure 7D). Halite (Figure 7E) and anhydrite (Figure 7F) are linearly aligned, presenting parallel bedding features in the field emission scanning electron microscopy images.

Interpretation—In comparison to the mudstone interlayers, the lower content of siliciclastic debris (e.g., quartz, feldspar) in lime mudstones (Figure 3A, B) suggests that the depositional environment was less influenced by terrigenous input. The lime mud- and clay-dominant laminae sets are interpreted as varve deposits. Specifically, the precipitation of the lacustrine

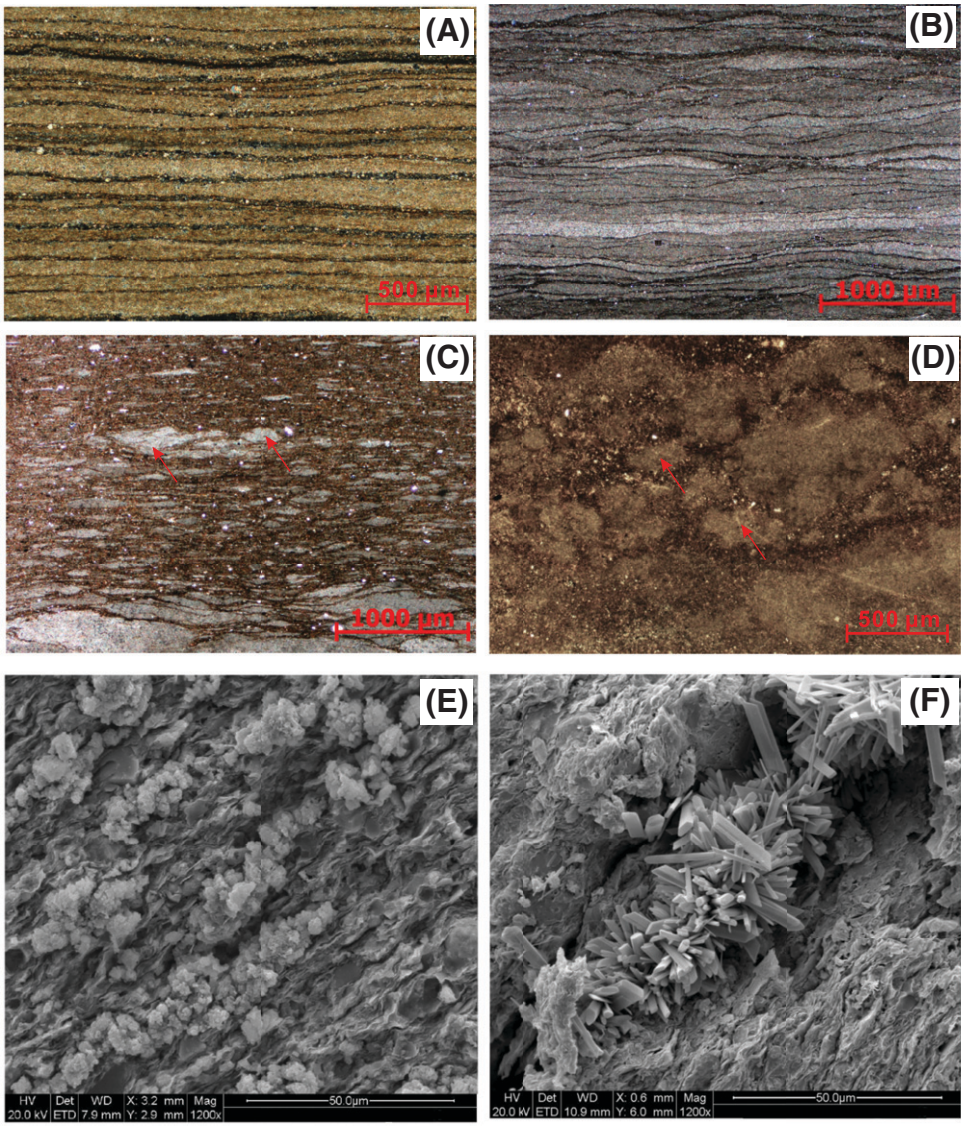

Figure 7. Petrological characteristics of lime mudstones of the middle Eocene Shahejie Formation in well Niuye1. See Figure 1B for the well location and Figure 8 for the stratigraphic locations of these photographs in the well. (A) Alternating microcrystalline calcite and clay laminae at 3359.87 m (11,023.20 ft). Mineralogical composition: clay = 9 wt. %, quartz = 8 wt. %, calcite = 77 wt. %, dolomite = 4 wt. %, pyrite = 1 wt. %, and gypsum = 1 wt. %. (B) Alternating microcrystalline calcite and clay laminae at 3362.25 m (11,031.00 ft). Mineralogical composition: clay = 5 wt. %, quartz = 5 wt. %, calcite = 89 wt. %, dolomite = 1 wt. %, and pyrite = 1 wt. %. (C) Lenticular microcrystalline calcite aggregates (red arrows), interpreted as bioturbation-related laminae, 3360.35 m (11,024.77 ft). (D) Mottling microcrystalline calcite aggregates (red arrows), interpreted as bioturbation-related laminae, 3366.80 m (11,045.93 ft). (E) Halite in the form of parallel bedding whose orientation is oblique to the horizontal direction; field emission scanning electron microscopy image, 3365.10 m (11,040.35 ft). (F) Anhydrite in the form of parallel bedding whose orientation is oblique to the horizontal direction; field emission scanning electron microscopy image, 3367.10 m (11,046.92 ft). Det ETD = detection Everhart-Thornley detector; HV = high voltage; Mag. = magnification; WD = working distance.

lime mud is postulated to have been induced by the photosynthetic activity of algae or bacteria, which increased the pH value and thus led to calcite precipitation in hardwater lakes (Robbins et al., 1997; Dittrich and Obst, 2004; Chagas et al., 2016; Gomez et al., 2018). The most spectacular seasonal $CaCO_3$ precipitation is seen in "whiting events" during summer, and these events are related to the exponential growth of microalgae or photosynthetic bacteria.

The summer-to-early autumn dinoflagellate blooms (see Zhang et al., 2021 for the dinoflagellate photographs) have been recorded in the lime

mudstones of the middle Eocene Dongying sag, and they are believed to have been the trigger for the precipitation of microcrystalline calcite (Zhang et al., 2019b). Thus, the microcrystalline calcite laminae should have formed during the warm seasons of a year. Halite and anhydrite (Figure 7E, F) are believed to have precipitated during peak summer, when the evaporation rate is the highest.

From late autumn to winter, the decreased lake temperature makes it difficult for dinoflagellate to survive, which, together with greater water saturability, prohibits microcrystalline calcite deposition. Meanwhile, some clay particles slowly settle out on the lake bottom, forming thin clay-rich laminae. Thus, the combination of microcrystalline calcite-rich and clay-rich laminae represents varve deposits.

Spore and Pollen Characteristics

Description—We adopted three parameters of spore and pollen to reconstruct the climate: (1) MAT, (2) mean temperature of the coldest months (CMT), and (3) mean temperature of the warmest months (WMT). The MAT reflects the most comfortable temperature zone for vegetation bloom; CMT and WMT reflect the temperature limitation. The combination of MAT and CMT and/or WMT thus reflect the influence of temperature on vegetation. In addition, Holdridge (1947) emphasizes the importance of the potential evaporation rate (*PER*; equation 1), as a humidity indicator, in dividing climatic zones.

$$PER = PET/P \tag{1}$$

$$PET = 58.93 \times BT \tag{2}$$

$$BT = \Sigma t/365 \text{ or } BT = \Sigma T/12 \tag{3}$$

where *PET* is abbreviated for the annual evaporation amount (in millimeters), *P* is the annual precipitation (in centimeters), *BT* is the annual average temperature of the vegetation (in degrees Celsius), *t* is the daily average temperature, and *T* is the monthly average temperature (the assignment is 30°C [86°F] if the temperature is higher than 30°C [86°F], whereas it is 0°C [32°F] if the temperature is lower than 0°C [32°F]).

Detailed MAT, CMT, WMT, and *PER* values of spore and pollen refer to the Paleoflora Database, in which spore and pollen types are divided into warm species, cold species, and temperature-insensitive species based on the adaptability of their parent plants to temperature. They are also classified into humid, arid, and humidity-insensitive species based on the adaptability of their parent plants to humidity.

According to the sensitivity of their parent plants to temperature and/or humidity, 18 types of spore and pollen are divided into warm and humid species (*Alsosporites* and *Toroisporites*); warm species (*Liquidambarpollenites*, *Quercoidites*, and *Rutaceoipollis*); cold and humid species (*Osmundacidites* and *Salixipollenites*); cold species (*Betulaceoipollenites*, *Juglanspollenites*, and *Ulmipollenites*); cold and arid species (*Ephedriptes* and *Labitricolpites*); and other genera that are insensitive to both temperature and humidity (*Abietineaepollenites*, *Abiespollenites*, *Cupuliferoipollenites*, *Lonicerapollis*, *Lycopodiumsporites*, and *Pinuspollenites*) (Table 2). In general, mudstones have a higher abundance of warm species and humid and warm species, whereas lime mudstones host more cold species and arid and cold species (Table 2).

Humidity index (*HI*) and temperature index (*TI*) are used with spore and/or pollen data from each sample to characterize the vertical climate changes (Figure 8). The calculation equations for *HI* and *TI* are as follows (Li et al., 2003):

$$HI = \frac{\textit{humid species abundance}}{\textit{humid species abundance} + \textit{arid species abundance}} \times \textit{spore and pollen abundance in a thin section} \tag{4}$$

$$TI = \frac{\textit{warm species abundance}}{\textit{warm species abundance} + \textit{cold species abundance}} \times \textit{spore and pollen abundance in a thin section.} \tag{5}$$

The two proxies vertically change at 2–3 m (6.56–9.84 ft) scales, keeping pace with the lithofacies changes (Figure 8). Accordingly, *HI* values in the mudstones (0.5–1, average 0.8) are higher than those in the lime mudstones (0.33–0.5, average 0.46). Meanwhile, *TI* values in the mudstones (0.4–0.8, average 0.69) are also higher than those in the lime mudstones (0.2–0.4, average 0.29).

Interpretation—Higher *HI* values would indicate higher humidity levels, whereas higher *TI* values would

Table 2. Spore and Pollen Species in the Interval of 3358–3380 m (11,017–11,089 ft) of Well Niuye1 of the Middle Eocene Shahejie Formation

		W&H		W			C&H		C			C&A					
Depth, m	Lithology	*Also.*	*Toroi.*	*Quer.*	*Ruta.*	*Liqui.*	*Sali.*	*Osmu.*	*Betu.*	*Jugla.*	*Ulmi.*	*Ephe.*	*Labi.*	Other Climate-Insensitive Genus	Total No.	*TI*	*HI*
3359.2	M	2	1				1							1	5	0.75	1.00
3360.3	LM		1							1			1	1	4	0.33	0.50
3361.4	M	2				1						1		3	7	0.75	0.67
3363.0	LM			1			1		1			1		3	7	0.25	0.50
3364.05	M	1		2						1				2	6	0.75	1.00
3365.3	LM					1		1				1	2	1	6	0.20	0.33
3366.3	M	1				3	2							2	8	0.67	1.00
3367.25	LM		1		1				1		2	1		3	9	0.33	0.50
3368.3	M	4	3			1			3				1	1	13	0.67	0.75
3369.45	LM		1		1		1					2		1	6	0.40	0.50
3370.6	M		1	2				1					1	1	6	0.60	0.67
3371.8	LM		1							1	1	2		3	8	0.20	0.33
3372.82	M		2				1		2					2	7	0.40	1.00
3373.45	LM	1						1				1		2	5	0.33	0.50
3374.9	M	1				3						1		3	8	0.80	0.50
3375.85	LM		1						1		1		1	2	6	0.25	0.50
3377.25	M	1	2	3					1			1		3	11	0.75	0.75
3378.1	LM	1							1			1		3	6	0.33	0.50
3378.6	M	1	1			1						1		2	6	0.75	0.67

See Figure 1B for well location. The other climate-insensitive genera include *Abiespollenites*, *Abietineaepollenites*, *Cupuliferoipollenites*, *Lonicerapollis*, *Lycopodiumsporites*, and *Pinuspollenites*. Warm and humid, cold and humid, and cold and arid species are sensitive to both temperature and humidity, whereas warm or cold species are sensitive only to temperature.

Abbreviations: A = arid; *Also.* = *Alsosporites*; *Betu.* = *Betulaceoipollenites*; C = cold; *Ephe.* = *Ephedriptes*; H = humid; *HI* = humidity index; *Jugla.* = *Juglanspollenites*; *Labi.* = *Labitricolpites*; *Liqui.* = *Liquidambarpollenites*; LM = lime mudstone; M = mudstone; *Osmu.* = *Osmundacidites*; *Quer.* = *Quercoidites*; *Sali.* = *Salixipollenites*; *TI* = temperature index; *Toroi.* = *Toroisporites*; *Ulmi.* = *Ulmipollenites*; W = warm.

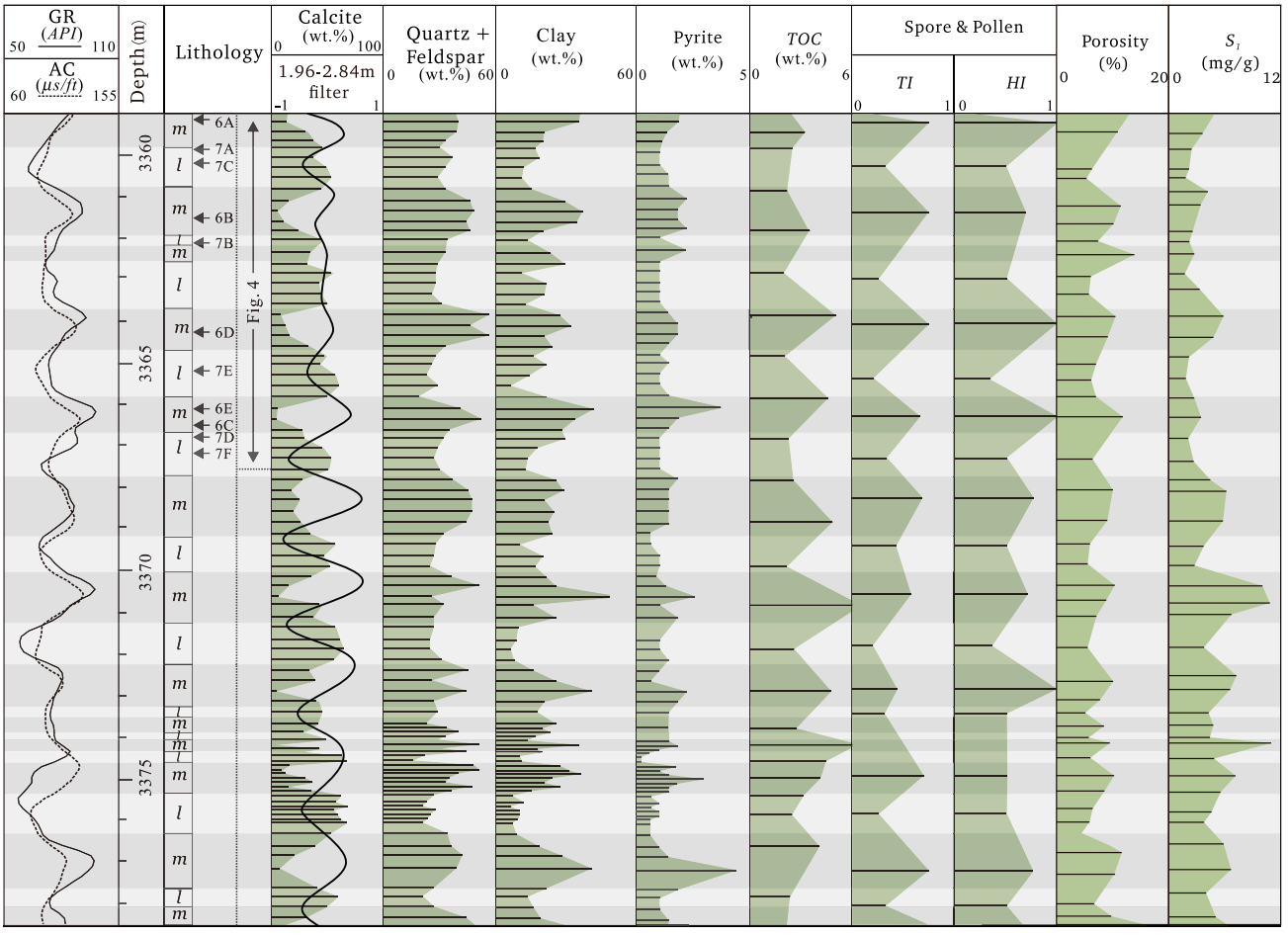

Figure 8. Integrated petrology, geochemistry, paleoecology, and meter-scale cycles for the interval of 3358 to 3380 m (11,017 to 11,089 ft) of the middle Eocene Shahejie Formation in well Niuye1. See Table 2 for a detailed calculation of temperature index (*TI*) and humidity index (*HI*). Photographs of the cores are shown in Figure 4. The arrows in the lithology column show the stratigraphic sampling locations in Figures 6 and 7. Note the robust cyclic signals for all of the proxies and how well these relate to lime mudstone-mudstone cycles, indicated by light gray and dark gray horizontal bars, respectively. The core depth was calibrated to well log depth through core spatial position restoring, with well log depth 0.6 m (1.97 ft) deeper than core depth. AC = acoustic log; GR = gamma ray; *l* = lime mudstone; *m* = mudstone; S_1 = amount of free hydrocarbons in Rock-Eval pyrolysis analysis; *TOC* = total organic carbon.

represent higher temperatures (Li et al., 2003). Thus, compared with lime mudstones, mudstones show higher *HI* and *TI* values and thus should be deposited in warmer and more humid climates. It shows that the mudstone–limestone couplets kept pace with climate changes, which is the basis for analyzing the relationship between mudstone–limestone couplets and Milankovitch cycles.

Reservoir Characteristics

Description—Mudstones and lime mudstones differ from each other in porosity, amount of free hydrocarbons (S_1), and rock brittleness. Porosity is found to be negatively correlated with the calcite content (coefficient of determination [R^2] = 0.62; Figure 9A) (see Liang et al., 2017 for scanning electron microscopy representation of the pores); porosity is 8.5%–17.8% (average 12.3%) in mudstones and 6.3%–12.1% (average 9.2%) in lime mudstones (Figures 8, 9A). The S_1 value is 3.9–11.3 mg/g (average 7.1 mg/g) in mudstones and 2.3–5.8 mg/g (average 3.9 mg/g) in lime mudstones because it is negatively correlated with the calcite content (R^2 = 0.59; Figures 8, 9B).

Among the dominant minerals in the mudstone–limestone couplets (e.g., quartz, feldspar, calcite, dolomite, pyrite, clay), only clay is ductile. Correspondingly, a higher clay content in mudstones (Figure 8) suggests a lower brittleness. In addition, vertical

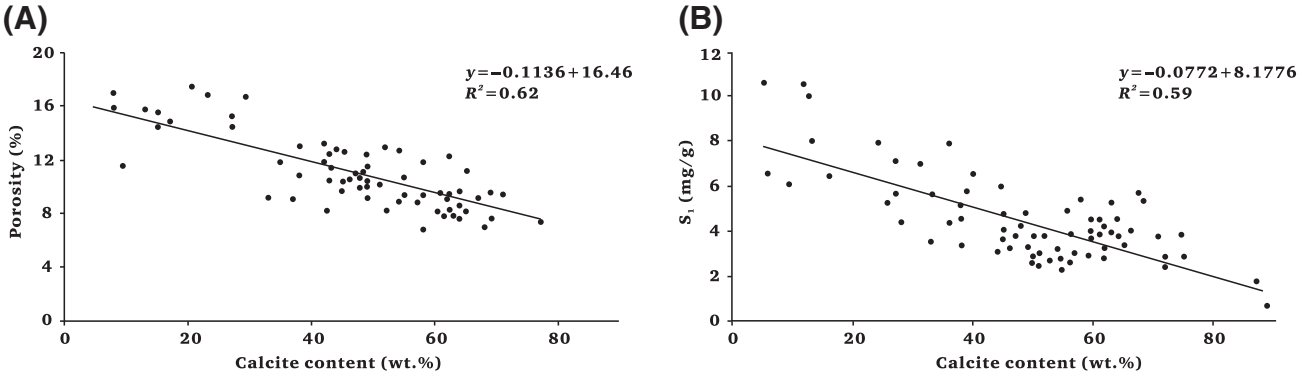

Figure 9. The crossplot showing (A) the relationship between the calcite content and porosity and (B) the relationship between the calcite content and the amount of free hydrocarbons in Rock-Eval pyrolysis analysis (S_1). R_2 = coefficient of determination.

cyclic changes occur in *TOC*, porosity, S_1, and brittleness, which keep pace with the 1.96- to 2.84-m filter (Figure 8).

Interpretation—The meter-scale mudstone–limestone couplets controlled the *TOC*, porosity, S_1, and brittleness of shale reservoir, resulting in meter-scale changes of shale reservoir properties. Mudstones have higher *TOC*, higher porosity, higher oil content, and lower rock brittleness in comparison to lime mudstones.

Cyclostratigraphic Characteristics

Procedure—The top and base of the upper Es_4 strata in the three wells were calibrated using volcanic ash layers (Yao et al., 2007a, b). Then, we determined our target depth intervals of the three wells by evolutional trends of the GR log. Next, the calibration of individual beds was completed through detailed characterization and correlation of bedding in the three wells. A total of 53 cycles were recognized using the GR data, which were respectively bounded by the peaks with the highest GR values and are numbered from 1 to 54 (Figure 5). The cycles were easy to define by mudstone–limestone couplets in cores (Figures 4, 5). To preclude the effect of local dynamics on our cyclostratigraphic analysis, a regionally averaged stratigraphic log curve was produced. Specifically, a preliminary, first-order correlation was implemented at a scale of approximately tens of meters, according to the features of the GR log curves, followed by further detailed correlation at meter scale (Figure 10).

Subsequently, the GR curves of the three wells were normalized and combined to generate a regionally averaged GR curve (Figure 10). The REDFIT power spectrum of the GR log (Figure 11) revealed three dominant peaks at periods of 2.4 m/cycle (7.9 ft/cycle), 3.7 m/cycle (12.1 ft/cycle), and 4.7 m/cycle (15.4 ft/cycle), with significance levels of >90% ($\alpha < 0.1$). Bandpass filtering of the average GR curve demonstrated a good one-to-one correlation between the 1.96- to 2.84-m (6.43–9.32 ft) filter and 50 GR cycles (Figure 10). Specifically, the GR peaks matched the minima of the 1.96- to 2.84-m (6.43–9.32 ft) filter, whereas the GR valleys corresponded to the maxima of the filter. The three not-well-related peaks (labeled as 5, 9, and 44 in Figure 10) matched maxima of the 2.84- to 5.32-m (9.32–17.45 ft) bandpass filter. In addition, GR values were significantly high in the intervals where peaks of the 1.96- to 2.84-m (6.43–9.32 ft) filter coincided with those of the 2.84- to 5.32-m (9.32–17.45 ft) filter.

Interpretation—The precession has three components (18.74, 21.92, and 23.08 k.y.), as does the obliquity (28.92, 39.49, and 51.32 k.y.) (Berger et al., 1992; Laskar et al., 2004, 2011) during deposition of our stratigraphy (42–45 Ma; Yao et al., 2007a, b). The ratio of the thickness of the 2.4-m (7.9-ft) cycle over that of the 4.7-m (15.4-ft) cycle is similar to the ratio of the 21.92 k.y. precession over the 39.49 k.y. obliquity (Table 3). The shorter 2.4-m (7.9-ft) GR cycle may relate to the precession cycle (Figure 10); the longer 4.7-m (15.4-ft) GR cycle should be related to the obliquity cycle; and the intermediate 3.7-m (12.1-ft) cycle would be attributable to a combination of both.

The dating of the series supports the above explanation. The studied upper Es_4 (Figure 1C) has an estimated duration of 3.0 m.y. (42–45 Ma; Yao et al.,

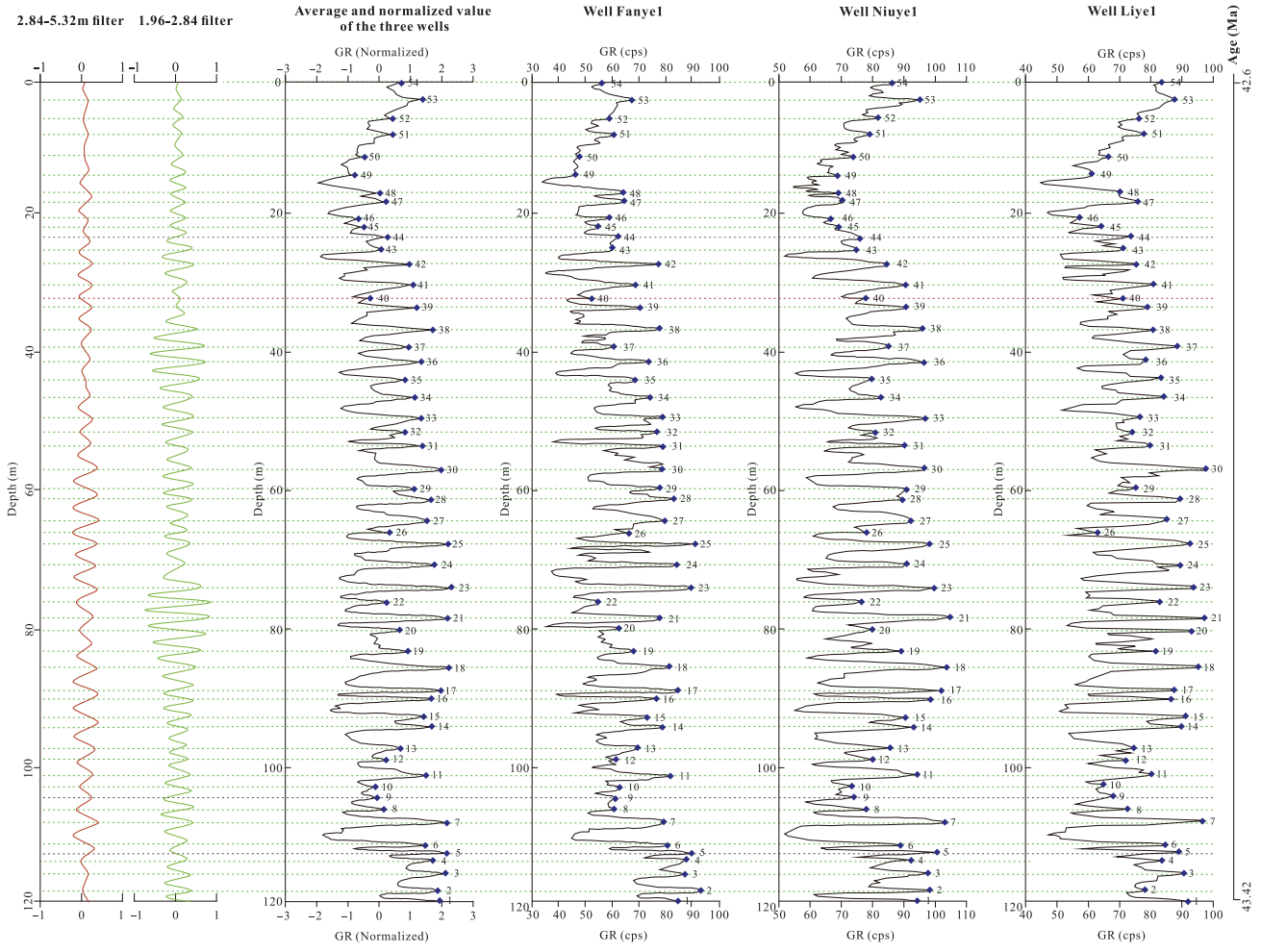

Figure 10. The tuned and normalized gamma ray (GR) curves. The normalized GR cycles are calculated from wells Fanye1, Liye1, and Niuye1. The normalized GR cycles generally match the 1.96–2.84 m (6.43–9.32 ft) filter. However, three additional cycles labeled 5, 9, and 44 exist in the normalized GR log, with their peaks matching those of the 2.84–5.32 m (9.32–17.45 ft) filter. cps = counts per second.

2007a, b) and thickness of approximately 350 m (~1148 ft) (3250–3600 m [10,663–11,811 ft]) Fanye1, 364 m (1194 ft) (3701–4065 m [12,142–13,337 ft]) Liye1, and 298 m (978 ft) (3316–3614 m [10,879–11,857 ft]) Niuye1 (Zhang, 2017). The duration of the studied interval in the three wells is calculated through interpolation, with the depositional rate assumed to be constant over the whole upper Es_4 (Figure 5). The studied interval then has an estimated duration of 1.12, 1.08, and 1.11 m.y. in wells Fanye1, Liye1, and Niuye1, respectively, and the regionally averaged stratigraphic log curve (Figure 10) has an estimated duration of 1.1 m.y. Thus, the average duration of the well-correlated 50 GR cycles (Figure 10) is 22 k.y., very close to the 21.92 k.y. precession periodicity.

Precession forcing of the dominant mudstone–limestone cyclicity also is based on the following observations: (1) these cycles are regularly alternating through time over a duration of more than 1.1 m.y., and (2) these cycles have laterally consistent thicknesses over distances of more than 73 km (45 mi) (Figures 1B, 5). In some intervals, every second precession cycle is enhanced, whereas in others the precession cycles are suppressed; this has been demonstrated to be precession-obliquity interference (Lourens et al., 2001). Dominance of the amplitude modulator of precession, eccentricity, seems absent in the studied interval. In cases in which eccentricity is low, precession and obliquity interference can be more clearly identified. It could be inferred that the target layers may have been deposited during a

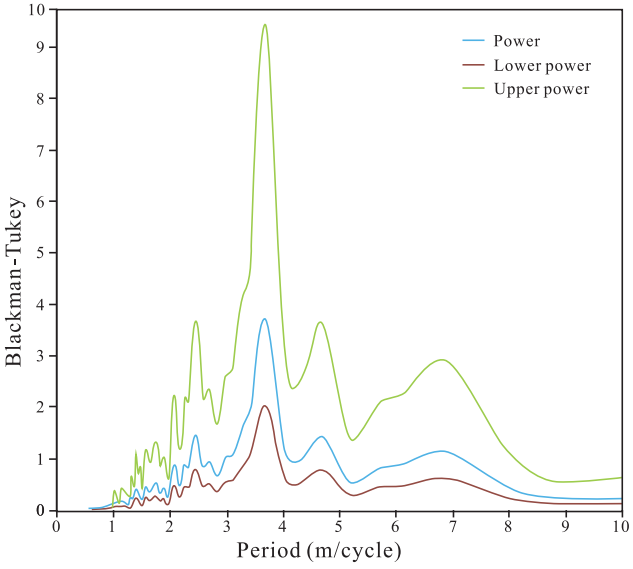

Figure 11. Blackman-Tukey power spectra of gamma ray data accompanied by the 90% upper and lower power spectra. Significantly obvious peaks at periods of approximately 2.4 m/cycle (7.9 ft/cycle), 3.7 m/cycle (12.1 ft/cycle), and 4.7 m/cycle (15.4 ft/cycle) are related to the observed mudstone–lime mudstone cyclicity in the cores.

long-period eccentricity low that is related to the 2.4-m.y. cycle, which explains the seemingly absent eccentricity and the relatively strong obliquity.

DISCUSSION

Orbital Climate Forcing of the Meter-Scale Mudrock Lithofacies Cyclicity

The above analysis shows that the observed mudstone–limestone cycles occur at periods that coincide with Milankovitch periodicities, and thus these cycles are believed to have been influenced by astronomically driven climate changes. The available age control and the ratio of cycle frequencies point to precession forcing of the meter-scale mudstone–limestone couplets and secondary imprints from obliquity. The phase relationship between orbital forcing and lithofacies cyclicity in our study area remains enigmatic and is discussed in the following sections.

Precession as the Primary Factor Controlling Meter-Scale Mudrock Lithofacies Cyclicity

Orbital forcing produces significant insolation differences (Berger et al., 1992), which can be up to 20% between two extremes of a precession cycle. Precession cycles have been proven to affect climate over various latitudes, including impacting monsoonal strength and influencing precipitation and temperature through the impact on insolation (Spicer et al., 2016).

In the northern hemisphere, previous case studies support the idea that higher monsoon strength and precipitation are generally in phase with the precession minimum, whereas lower monsoon strength and precipitation occur during precession maximum. For example, in the modern African and Asian monsoon systems, strengthened summer monsoon and precipitation are observed during precession minima, which is attributed to the increased summer insolation that intensifies the airflow convection between the ocean and continent; in contrast, the summer monsoon and precipitation become lower and desert expands as a result of low summer insolation during precession maxima (Tuenter et al., 2003, 2007).

Similarly, the coupled ocean–atmosphere weather model ECBilt by Bosmans (2014) also shows the correspondence of higher average precipitation and intensified monsoon activity to precession minima in the northeast part of Asia, which is interpreted to be caused by the difference between the ocean and continent in the airflow convection strength (Abels and Ziegler, 2018). In addition, humid conditions are suggested to occur during precession minima based on the sedimentary records in the Miocene Abad Formation, the Sorbas Basin, southern Spain (Sierro et al., 1999). These case studies support our explanations in the Dongying sag. In the present study, precession minima are interpreted to have been responsible for mudstone deposition, whereas

Table 3. Proportional Relation between Gamma Ray Cycle Thickness and Orbital Cycle Period in the Middle Eocene

The Tuned and Normalized Well in Figure 10		Orbital Cycle	
GR Cycle Thickness, m	Ratio	Duration, k.y.	Ratio
2.44	1	21.92	1
3.68	1.51	*	*
4.67	1.91	39.49	1.80

Abbreviation: GR = gamma ray.
*The GR Cycle Thickness of 3.68 m was forced by the combination of 21.92 k.y. and 39.49 k.y. in orbital cycles.

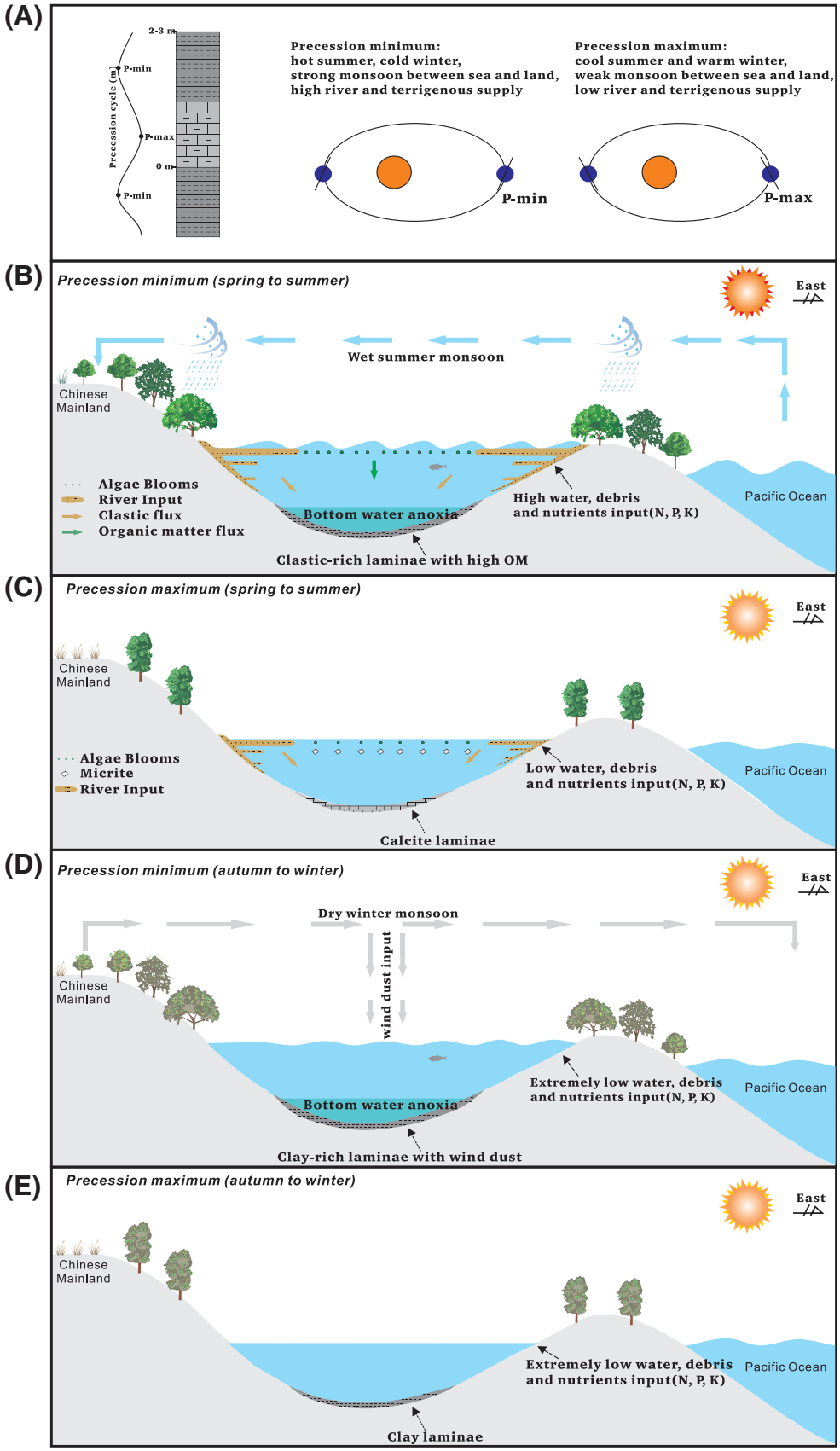

Figure 12. Conceptual model for precession-driven climate control on mudrock deposition in East Asia during the middle Eocene. K = kalium; max = maximum; min = minimum; N = nitrogen; OM = organic matter; P = phosphorus.

precession maxima are held responsible for lime mudstone deposition (Figure 12A).

Deposition in the middle Eocene Dongying sag is suggested to have occurred under a monsoonal climate system (Licht et al., 2014; Quan et al., 2014; Ma et al., 2019). (See Figure 1A and the Climate Setting section for a detailed description.) During the summer seasons of the precession minima, higher summer insolation caused lower atmospheric pressure above the Asian mainland, triggering in tensified landward summer monsoon from the subtropical ocean. The intensified summer monsoon enhanced humid air flow, causing higher precipitation. Increased precipitation is interpreted to cause higher lake levels and increased siliciclastic input due to higher discharge through the feeding rivers (Figure 12B). This caused deposition of siliciclastic laminae in mudstones (Figures 6A–D; 12B). In contrast, in summer seasons of precession maxima, the relatively decreased summer insolation resulted in a relatively weak monsoon and lower precipitation and river discharge (Figure 12C). Lower terrigenous input and river discharge led to the deposition of microcrystalline calcite laminae in lime mudstones (Figure 12C).

During the winter seasons of the precession minima, the lower winter insolation caused higher atmospheric pressure above the Asian mainland, causing a moisture-poor seaward winter monsoon from the Asia inland (Figure 12D, E). The occurrence of widespread wind dust from the Chinese loess plateau (Figure 6E, F) in the clay laminae of mudstones rather than lime mudstones suggests that the mudstones were deposited in environments having intensified winter monsoon during precession minima (Figure 12D, E). Because the seaward winter monsoon from the inland carried little moisture, winter precipitation was extremely low in both precession minima and maxima, in line with modeling findings (Tuenter et al., 2003). The low winter precipitation and thus the low river discharge resulted in the deposition of clay laminae (Figure 12D, E) in both precession minimum and maximum.

Obliquity as the Secondary Factor Controlling Lithofacies Cyclicity

Obliquity imprinted the middle Eocene Bohai Bay basin to a lesser extent. The vertically alternating higher and lower GR peaks (Figure 10) are seemingly products of precession–obliquity interference, and a few standalone peaks (labeled as 5, 9, and 44 in Figure 10) that do not match precession cycles seem to represent obliquity cycles.

Previous case studies have shown the strong impact of obliquity on monsoonal systems and accompanied precipitation (Li et al., 2017). For example, the combined effects of precession and obliquity forcing have been recorded in the Asian monsoon (Caley et al., 2011), the African monsoon (Tuenter et al., 2003), and the Australian monsoon (Wyrwoll et al., 2007). In the summer monsoon system of Holocene Africa, obliquity intensified precipitation during its maxima and weakened precipitation during its minima (Tuenter et al., 2003).

We propose that obliquity cycles influenced mudrock lithofacies cyclicity by controlling the monsoon system and precipitation in our study area. The monsoon system in our study area is formed by the airflow convection between the high-latitude Siberian plateau and the low-latitude subtropical Pacific Ocean (Figure 1A). Because the influence of obliquity on summer insolation is stronger in high latitudes than in low latitudes (Liu, 1995; Barke et al., 2011), a higher gradient of summer insolation (obliquity maximum) can introduce a lower atmospheric pressure above the Siberian plateau, and thus a greater pressure contrast between the continent and ocean; in this context, stronger southeast moisture-rich monsoon blows from the ocean toward the Dongying sag. Consequently, the precipitation increases, followed by changes in terrigenous input and water salinity. In contrast, a lower gradient of summer insolation (obliquity minimum) causes lowered precipitation, which results in opposite effects on terrigenous input, and water salinity.

Orbital Forcing–Paced Shale Reservoir Quality Heterogeneity

The hydrocarbon exploration and exploitation in the Dongying sag are significantly affected by the vertical shale reservoir heterogeneity. Knowledge of the controls of vertical heterogeneity is thus crucial to predict reservoir properties. In the present study, orbital forcing is demonstrated to have been a dominant control not only on the depositional environmental evolution but also on the vertical shale reservoir heterogeneity. Precession, and to a lesser extent, obliquity, are found to control several factors that are key to shale reservoir exploration and exploitation, including *TOC*,

porosity, S_1, and brittleness (Figures 9, 10). As the amplitude of precession is controlled by eccentricity, we anticipate that eccentricity is a critical control on the larger-scale vertical reservoir character. Allogenic forcing of mudstone–limestone cyclicity implies a continuous bedding of layers with better and less good reservoir properties over vast distances. This means that vertical reservoir connectivity, and thus vertical permeability, is lower than when beds are driven by autogenic forcing. Cyclostratigraphic analysis is an effective method to reveal the high-resolution meter-scale shale and potentially decameter-scale reservoir heterogeneity. It is helpful and conducive in the shale oil exploration of middle Eocene Dongying sag, as well as shale oil and gas exploration in other basins with a similar background.

CONCLUSIONS

The upper Es_4 mudrock in the Dongying sag is characterized by meter-scale mudstone–limestone couplets with thickness ranges of 0.7 to 6 m (average 2.33 m) (2.30–19.69 ft [average 7.64 ft]) and a standard deviation of 0.4 m (1.3 ft). Compared with lime mudstones, mudstones were deposited in warmer and more humid climates. These couplets are laterally continuous, and they can be well correlated in three wells having a lateral distance of 73 km (45.4 mi).

These couplets occur at periods that coincide with Milankovitch periodicities and patterns. Age control suggests that the deposition of the couplets was primarily driven by precession cycles, with additional imprint of the obliquity forcing. Each precession cycle matches one mudstone–limestone couplet. The increased summer insolation during the precession minimum increases the summer monsoonal precipitation, thereby increasing surface discharge and terrigenous input. This results in the deposition of siliciclastic-rich mudstones in the basin. Decreased summer insolation during precession maxima decreases the summer monsoonal precipitation, the surface discharge, and the terrigenous input, while increasing the water salinity, which is accompanied by the formation of authigenic lime mudstones.

The Milankovitch cycles determine the deposition of mudstone–limestone couplets and thus determine shale reservoir quality, controlling the high-frequency cyclic changes of shale reservoir heterogeneity at a scale of approximately 2–3 m (6.56–9.84 ft). Mudstones deposited during the precession (21.92 k.y.) minima have higher *TOC*, higher porosity, higher oil content, and lower rock brittleness in comparison to lime mudstones deposited during the precession (21.92 k.y.) maxima. The orbital forcing model probably implies lower vertical permeability than if autogenic processes would have been the dominant drivers of lacustrine deposition in the Bohai Bay Basin.

REFERENCES CITED

Abels, H. A., and M. Ziegler, 2018, Paleoclimate, *in* C. Hoorn, A. Perrigo, and A. Antonelli, eds., Mountains, climate and biodiversity: New York, John Wiley & Sons, p. 123–134.

Allen, M. B., D. I. M. Macdonald, Z. Xun, S. J. Vincent, and C. Brouet-Menzies, 1997, Early Cenozoic two-phase extension and late Cenozoic thermal subsidence and inversion of the Bohai Basin, northern China: Marine and Petroleum Geology, v. 14, p. 951–972, doi:10.1016/S0264-8172(97)00027-5.

Barke, J., H. A. Abels, F. Sangiorgi, D. R. Greenwood, A. R. Sweet, T. Donders, G. Reichart, A. F. Lotter, and H. Brinkhuis, 2011, Orbitally forced *Azolla* blooms and middle Eocene Arctic hydrology: Clues from palynology: Geology, v. 39, no. 5, p. 427–430, doi:10.1130/G31640.1.

Berger, A., M. F. Loutre, and J. Laskar, 1992, Stability of the astronomical frequencies over the Earth's history for paleoclimate studies: Science, v. 255, no. 5044, p. 560–566, doi:10.1126/science.255.5044.560.

Bishop, J. K. B., R. E. Davis, and J. T. Sherman, 2002, Robotic observations of dust storm enhancement of carbon biomass in the North Pacific: Science, v. 298, no. 5594, p. 817–821, doi:10.1126/science.1074961.

Bosmans, J. H. C., 2014, A model perspective on orbital forcing of monsoons and Mediterranean climate using EC-Earth. Ph.D. thesis, Utrecht University, Utrecht, the Netherlands, 159 p.

Caley, T., B. Malaize, M. Revel, E. Ducassou, K. Wainer, M. Ibrahim, D. Shoeaib, S. Migeon, and V. Marieu, 2011, Orbital timing of the Indian, East Asian and African boreal monsoons and the concept of a "global monsoon": Quaternary Science Reviews, v. 30, no. 25, p. 3705–3715, doi:10.1016/j.quascirev.2011.09.015.

Cantalejo, B., and K. T. Pickering, 2014, Climate forcing of fine-grained deep-marine systems in an active tectonic setting: Middle Eocene, Ainsa Basin, Spanish Pyrenees: Palaeogeography, Palaeoclimatology, Palaeoecology, v. 410, p. 351–371, doi:10.1016/j.palaeo.2015.01.008.

Cantalejo, B., and K. T. Pickering, 2015, Orbital forcing as principal driver for fine-grained deep-marine siliciclastic sedimentation, middle Eocene Ainsa Basin, Spanish Pyrenees: Palaeogeography, Palaeoclimatology, Palaeoecology, v. 421, p. 24–47, doi:10.1016/j.earscirev.2016.09.012.

Chagas, A. P., G. E. Webb, R. V. Burne, and G. Southam, 2016, Modern lacustrine microbialites: Towards a synthesis of aqueous and carbonate geochemistry and mineralogy: Earth-Science Reviews, v. 162, p. 338–363, doi:10.1016/S0037-0738(97)00076-6.

D'Argenio, B., V. Ferreri, S. Amodio, and N. Pelosi, 1997, Hierarchy of high-frequency orbital cycles in Cretaceous carbonate platform strata: Sedimentary Geology, v. 113, p. 169–193, doi:10.1016/S0037-0738(97)00076-6.

Dittrich, M., and M. Obst, 2004, Are picoplankton responsible for calcite precipitation in lakes?: Ambio, v. 33, no. 8, p. 559–564, doi:10.1579/0044-7447-33.8.559.

Eldrett, J. S., C. Ma, S. C. Bergman, A. Ozkan, D. Minisini, B. Lutz, S. Jackett, C. Macaulay, and A. E. Kelly, 2015, Origin of limestone-marlstone cycles: Astronomic forcing of organic-rich sedimentary rocks from the Cenomanian to early Coniacian of the Cretaceous Western Interior Seaway, USA: Earth and Planetary Science Letters, v. 423, p. 98–113, doi:10.1016/j.epsl.2015.04.026.

Goldhammer, R. K., and M. T. Harris, 1989, Eustatic controls on the stratigraphy and geometry of the Latemar Buildup (middle Triassic), the dolomites of northern Italy, *in* P. D. Crevello, J. L. Wilson, J. F. Sarg, and J. F. Read, eds., Controls on carbonate platforms and basin development: Tulsa, Oklahoma, SEPM Special Publication 44, p. 323–338, doi:10.2110/pec.89.44.0323.

Goldhammer, R. K., E. J. Oswald, and P. A. Dunn, 1994, High-frequency, glacio-eustatic cyclicity in the Middle Pennsylvanian of the Paradox Basin: An evaluation of Milankovitch forcing, *in* P. L. Boer and D. G. Smith, eds., Orbital forcing and cyclic sequences: Oxford, United Kingdom, Blackwell Scientific Publications, p. 243–283, doi:10.1002/9781444304039.ch18.

Gomez, F. J., C. Mlewski, F. J. Boidi, M. E. Farías, and E. Gérard, 2018, Calcium carbonate precipitation in diatom-rich microbial mats: The Laguna Negra hypersaline lake, Catamarca, Argentina: Journal of Sedimentary Research, v. 88, no. 6, p. 727–742, doi:10.2110/jsr.2018.37.

Herbert, T. D., and A. G. Fischer, 1986, Milankovitch climatic origin of mid-Cretaceous black shale rhythms in central Italy: Nature, v. 321, no. 6072, p. 739–743, doi:10.1038/321739a0.

Hinnov, L. A., and R. K. Goldhammer, 1991, Spectral analysis of the Middle Triassic Latemar Limestone: Journal of Sedimentary Petrology, v. 61, p. 1173–1193.

Holdridge, L. R., 1947, Determination of world plant formations from simple climatic data: Science, v. 105, no. 2727, p. 367–368, doi:10.1126/science.105.2727.367.

Hüsing, S. K., A. Beniest, A. Van der Boon, H. A. Abels, M. H. L. Deenen, M. Ruhl, and W. Krijgsman, 2014, Astronomically-calibrated magnetostratigraphy of the lower Jurassic marine successions at St. Audrie's Bay and East Quantoxhead (Hettangian-Sinemurian; Somerset, UK): Palaeogeography, Palaeoclimatology, Palaeoecology, v. 403, p. 43–56, doi:10.1016/j.palaeo.2014.03.022.

Jiang, Z., 2017, Paleogene sedimentary system and sedimentary dynamics of windfield-source-basin system in the Dongying Sag, *in* Z. Jiang, ed., Sedimentary dynamics of Windfield-Source-Basin System: New York, Springer, p. 121–204.

Jiang, Z., D. Chen, L. Qiu, H. Liang, and J. Ma, 2007, Source-controlled carbonates in a small Eocene half-graben lake basin (Shulu sag) in central Hebei province, north China: Sedimentology, v. 54, p. 265–292, doi:10.1111/j.1365-3091.2006.00834.x.

Kauffman, E. G., W. P. Elder, and B. B. Sageman, 1991, Advances and limits of high-resolution event stratigraphy (HIRES), *in* G. Einsele, A. Seilacher, and W. Ricken, eds., Cycles and events in stratigraphy: Berlin, Springer-Verlag, 795–819.

Kietzmann, D. A., J. Martín-Chivelet, R. M. Palma, J. López-Gómez, M. Lescano, and A. Concheyro, 2011, Evidence of precessional and eccentricity orbital cycles in a Tithonian source rock: The mid-outer carbonate ramp of the Vaca Muerta Formation, northern Neuquén Basin, Argentina: AAPG Bulletin, v. 95, no. 9, p. 1459–1474, doi:10.1306/01271110084.

Kietzmann, D. A., R. M. Palma, and M. P. I. Llanos, 2015, Cyclostratigraphy of an orbitally-driven Tithonian-Valanginian carbonate ramp succession, Southern Mendoza, Argentina: Implications for the Jurassic–Cretaceous boundary in the Neuquén Basin: Sedimentary Geology, v. 315, p. 29–46, doi:10.1016/j.sedgeo.2014.10.002.

Kominz, M. A., 1996, Whither cyclostratigraphy? Testing the gamma method on upper Pleistocene deep-sea sediments, North Atlantic Deep Sea Drilling Project Site 609: Paleoceanography, v. 11, p. 481–504, doi:10.1029/96PA00812.

Lapointe, F., P. Francus, S. F. Lamoureux, M. Said, and S. Cuven, 2012, 1750 years of large rainfall events inferred from particle size at East Lake, Cape Bounty, Melville Island, Canada: Journal of Paleolimnology, v. 48, no. 1, p. 159–173, doi:10.1007/s10933-012-9611-8.

Laskar, J., A. Fienga, M. Gastineau, and H. Manche, 2011, La2010: A new orbital solution for the long-term motion of the Earth: Astronomy & Astrophysics, v. 532, p. 1–15.

Laskar, J., P. Robutel, F. Joutel, M. Gastineau, A. C. M. Correia, and B. Levrard, 2004, A long-term numerical solution for the insolation quantities of the Earth: Astronomy & Astrophysics, v. 428, p. 261–285, doi:10.1051/0004-6361/201116836.

Lei, H., Z. Jiang, and H. Zhou, 2018, Analysis of paleoclimate evolution of the hyperthermal period in the early Paleogene: Taking Dongying Depression as an example [in Chinese with English abstract]: Earth Science Frontiers, v. 25, no. 4, p. 176–184.

Li, S., M. Wang, D. Zheng, and X. Zhao, 2003, Recovery of climate of Palaeogene in Jiyang Depression of Shandong [in Chinese with English abstract]: Journal of Shandong University of Science and Technology, v. 22, p. 6–9.

Li, T., F. Liu, H. A. Abels, C. You, Z. Zhang, J. Chen, J. Ji, et al., 2017, Continued obliquity pacing of East Asian summer precipitation after the mid-Pleistocene transition: Earth and Planetary Science Letters, v. 457, p. 181–190, doi:10.1016/j.epsl.2016.09.045.

Liang, C., Y. Cao, Z. Jiang, J. Wu, G. Song, and Y. Wang, 2017, Shale oil potential of lacustrine black shale in the

Eocene Dongying depression: Implications for geochemistry and reservoir characteristics: AAPG Bulletin, v. 101, p. 1835–1858, doi:10.1306/01251715249.

Licht, A., M. van Cappelle, H. A. Abels, J. B. Ladant, J. Trabucho-Alexandre, C. France-Lanord, Y. Donnadieu, et al., 2014, Asian monsoons in a late Eocene greenhouse world: Nature, v. 513, no. 7519, p. 501–506, doi:10.1038/nature13704.

Liu, H., 1995, A new view on the driving mechanism of Milankovitch glaciation cycles: Earth and Planetary Science Letters, v. 131, p. 17–26, doi:10.1016/0012-821X(95)00008-Z.

Lourens, L. J., R. Wehausen, and H. J. Brumsack, 2001, Geological constraints on tidal dissipation and dynamical ellipticity of the Earth over the past three million years: Nature, v. 409, no. 6823, p. 1029–1033, doi:10.1038/35059062.

Lu, H., and Z. An, 1999, Comparison of grain-size distribution of red clay and loess paleosol deposits in Chinese Loess Plateau [in Chinese with English abstract]: Acta Sedimentologica Sinica, v. 17, no. 2, p. 226–232.

Ma, Y., M. Fan, and Y. Lu, 2019, Stable isotope record of middle Eocene monsoon and its instability in eastern China: Global and Planetary Change, v. 175, p. 103–112, doi:10.1016/j.gloplacha.2019.02.007.

Macquaker, J. H. S., K. G. Taylor, M. Keller, and D. Polya, 2014, Compositional controls on early diagenetic pathways in fine-grained sedimentary rocks: Implications for predicting unconventional reservoir attributes of mudstones: AAPG Bulletin, v. 98, no. 3, p. 587–603, doi:10.1306/08201311176.

Meyers, S. R., 2008, Resolving Milankovitchian controversies: The Triassic Latemar Limestone and the Eocene Green River Formation: Geology, v. 36, p. 319–322, doi:10.1130/G24423A.1.

Michalzik, D., 1996, Lithofacies, diagenetic spectra and sedimentary cycles of Messinian (late Miocene) evaporites in SE Spain: Sedimentary Geology, v. 106, p. 203–222, doi:10.1016/S0037-0738(96)00007-3.

Ministry of Natural Resources, People's Republic of China, 2020, Annual report of China mineral resources [in Chinese], Beijing, China, Geological Publishing House, accessed June 9, 2022, http://www.mnr.gov.cn/sj/sjfw/kc_19263/zgkczybg/202010/t20201022_2572964.html.

Paillard, D. L., L. Labeyrie, and P. Yiou, 1996, Macintosh program performs time-series analysis: Eos, v. 77, p. 379, doi:10.1029/96EO00259.

Pillans, B., J. Chappell, and T. Naish, 1998, A review of the Milankovitch climatic beat: Template for Plio-Pleistocene sea-level changes and sequence stratigraphy: Sedimentary Geology, v. 122, p. 5–21, doi:10.1016/S0037-0738(98)00095-5.

Plint, A. G., J. H. S. Macquaker, and B. L. Varban, 2012, Bedload transport of mud across a wide, storm-influenced ramp: Cenomanian–Turonian Kaskapau Formation, western Canada foreland basin: Journal of Sedimentary Research, v. 82, p. 801–822, doi:10.2110/jsr.2012.64.

Poletti, L., I. P. Silva, D. Masetti, M. Pipan, and M. Claps, 2004, Orbitally driven fertility cycles in the Palaeocene pelagic sequences of the Southern Alps (Northern Italy): Sedimentary Geology, v. 164, p. 35–54, doi:10.1016/j.sedgeo.2003.09.001.

Potter, P. E., J. B. Maynard, and P. J. Depetris, 2005, Mud and mudstones: New York, Springer, 232 p., doi:10.1007/b138571.

Quan, C., Z. Liu, T. Utescher, J. Jin, J. Shu, Y. Li, and Y. Liu, 2014, Revisiting the Paleogene climate pattern of East Asia: A synthetic review: Earth-Science Reviews, v. 139, p. 213–230, doi:10.1016/j.earscirev.2014.09.005.

Ricken, W., 1996, Bedding rhythms and cyclic sequences as documented in organic carbon carbonate patterns, upper Cretaceous, Western Interior, US: Sedimentary Geology, v. 102, p. 131–154, doi:10.1016/0037-0738(95)00060-7.

Ridge, J. C., G. Balco, R. L. Bayless, C. C. Beck, L. B. Carter, J. L. Dean, E. B. Voytek, and J. H. Wei, 2012, The new North American Varve Chronology: A precise record of southeastern Laurentide Ice Sheet deglaciation and climate, 18.2-12.5 kyr BP, and correlations with Greenland ice core records: American Journal of Science, v. 312, no. 7, p. 685–722, doi:10.2475/07.2012.01.

Robbins, L. L., Y. Tao, and C. A. Evans, 1997, Temporal and spatial distribution of whitings on Great Bahama Bank and a new lime mud budget: Geology, v. 25, no. 10, p. 947–950, doi:10.1130/0091-7613(1997)025<0947:TASDOW>2.3.CO;2.

Sageman, B. B., and M. A. Arthur, 1994, Early Turonian paleogeographic/paleobathymetric map, Western Interior, US, *in* M. V. Caputo, J. A. Peterson, and K. J. Franczyk, eds., Mesozoic systems of the Rocky Mountain region, USA: Denver Colorado, SEPM Rocky Mountain Section, p. 457–470.

Schieber, J., 2016, Mud re-distribution in epicontinental basins: Exploring likely processes: Marine and Petroleum Geology, v. 71, p. 119–133, doi:10.1016/j.marpetgeo.2015.12.014.

Schimmelmann, A., C. B. Lange, and J. Schieber, 2016, Varves in marine sediments: A review: Earth-Science Reviews, v. 159, p. 215–246, doi:10.1016/j.earscirev.2016.04.009.

Schulz, M., and M. Mudelsee, 2002, REDFIT: Estimating red noise spectra directly from unevenly spaced paleoclimatic time series: Computers & Geosciences, v. 28, p. 421–426, doi:10.1016/S0098-3004(01)00044-9.

Scotchman, J. I., K. T. Pickering, C. Sutcliffe, N. Dakin, and E. Armstrong, 2015, Milankovitch cyclicity within the middle Eocene deep-marine Guaso System, Ainsa Basin, Spanish Pyrenees: Earth-Science Reviews, v. 144, p. 107–121, doi:10.1016/j.earscirev.2015.01.007.

Sierro, F. J., J. A. Flores, and I. Zamarreno, 1999, Messinian pre-evaporite sapropels and precession-induced oscillations in western Mediterranean climate: Marine Geology, v. 153, p. 137–146, doi:10.1016/S0025-3227(98)00085-1.

Song, M., H. Liu, Y. Wang, and Y. Liu, 2020, Enrichment rules and exploration practices of Paleogene shale oil in Jiyang Depression, Bohai Bay Basin, China [in Chinese with English abstract]: Petroleum Exploration and Development, v. 47, no. 2, p. 225–235, doi:10.1016/S1876-3804(20)60043-X.

Spicer, R. A., J. Yang, A. B. Herman, T. Kodrul, N. Maslova, T. E. Spicer, G. Aleksandrova, and J. Jin, 2016, Asian

Eocene monsoons as revealed by leaf architectural signatures: Earth and Planetary Science Letters, v. 449, p. 61–68, doi:10.1016/j.epsl.2016.05.036.

Strasser, A., F. J. Hilgen, and P. H. Heckel, 2006, Cyclostratigraphy - concepts, definitions, and applications: Newsletters on Stratigraphy, v. 42, no. 2, p. 75–114, doi:10.1127/0078-0421/2006/0042-0075.

Su, C., F. Li, X. Tan, X. Gong, K. Zeng, H. Tang, M. Li, and X. Wang, 2020, Recognition of diagenetic contribution to the formation of limestone-marl alternations: A case study from Permian of south China: Marine and Petroleum Geology, v. 111, p. 765–785, doi:10.1016/j.marpetgeo.2019.08.033.

Tateo, F., N. Morandi, A. Nicolai, M. Ripepe, R. Coccioni, S. Galeotti, and F. Baudin, 2000, Orbital control on pelagic clay sedimentology: The case of the late Albian "Amadeus Segment" (central Italy) [in French with English abstract]: Bulletin de la Société Géologique de France, v. 171, no. 2, p. 217–228, doi:10.2113/171.2.217.

Tuenter, E., S. L. Weber, F. J. Hilgen, and L. Lourens, 2003, The response of the African summer monsoon to remote and local forcing due to precession and obliquity: Global and Planetary Change, v. 36, p. 219–235, doi:10.1016/S0921-8181(02)00196-0.

Tuenter, E., S. L. Weber, F. J. Hilgen, and L. Lourens, 2007, Simulating sub-Milankovitch climate variations associated with vegetation dynamics: Climate of the Past, v. 3, p. 169–180, doi:10.5194/cp-3-169-2007.

Tylmann, W., and B. Zolitschka, 2020, Annually laminated lake sediments—Recent progress: Quaternary, v. 3, doi:10.3390/quat3010005.

Wang, G., 2007, Identification of aeolian silty sand in lacustrine shale of the Shahejie Formation in the Jiyang Depression and its indication to Paleoclimate [in Chinese with English abstract]: Acta Geologica Sinica, v. 81, p. 413–418.

Westphal, H., M. J. Head, and A. Munnecke, 2000, Differential diagenesis of rhythmic limestone alternations supported by palynological evidence: Journal of Sedimentary Research, v. 70, p. 715–725, doi:10.1306/2DC40932-0E47-11D7-8643000102C1865D.

Westphal, H., and A. Munnecke, 2003, Limestone-marl alternations: A warm-water phenomenon?: Geology, v. 31, p. 263–266, doi:10.1130/0091-7613(2003)031<0263:LMAAWW>2.0.CO;2.

Wyrwoll, K. H., Z. Liu, G. Chen, J. E. Kutzbach, and X. Liu, 2007, Sensitivity of the Australian summer monsoon to tilt and precession forcing: Quaternary Science Reviews, v. 26, no. 25, p. 3043–3057, doi:10.1016/j.quascirev.2007.06.026.

Xu, W., M. Ruhl, S. P. Hesselbo, J. B. Riding, and H. C. Jenkyns, 2017, Orbital pacing of the early Jurassic carbon cycle, black shale formation and seabed methane seepage: Sedimentology, v. 64, p. 127–149, doi:10.1111/sed.12329.

Yang, R., A. Fan, Z. Han, and A. J. Van Loon, 2017a, Lithofacies and origin of the late Triassic muddy gravity-flow deposits in the Ordos Basin, central China: Marine and Petroleum Geology, v. 85, p. 194–219, doi:10.1016/j.marpetgeo.2017.05.005.

Yang, R., Z. Jin, A. J. Van Loon, Z. Han, and A. Fan, 2017b, Climatic and tectonic controls of lacustrine hyperpycnite origination in the late Triassic Ordos Basin, central China: Implications for unconventional petroleum development: AAPG Bulletin, v. 101, no. 1, p. 95–117, doi:10.1306/06101615095.

Yao, Y. M., D. Y. Xu, and Y. Han, 2007a, Astrostratigraphic age analysis of the Eocene-Oligocene boundary in the Jiyang Sag, Shandong [in Chinese with English abstract]: Journal of Stratigraphy, v. 31, p. 483–494.

Yao, Y. M., D. Y. Xu, and B. L. Li, 2007b, High resolution cyclostratigraphic study on the third member of Shahejie formation of drill core Niu38 in the Dongying Depression [in Chinese with English abstract]: Shandong Province Journal of Stratigraphy, v. 31, p. 229–239.

Zhang, J., 2017, The formation mechanisms of lacustrine fine-grained sedimentary rocks in the Eocene lower Es_3 strata, the Jiyang Depression [in Chinese with English abstract], Ph.D. thesis, China University of Geosciences, Beijing, China, 154 p.

Zhang, J., Z. Jiang, E. Gierlowski-Kordesch, B. Xian, Z. Li, S. Wang, and X. Wang, 2017, A double-cycle lake basin formed in extensional to transtensional setting: The Paleogene Nanpu Sag, Bohai Bay Basin, China: Sedimentary Geology, v. 349, p. 15–32, doi:10.1016/j.sedgeo.2016.12.006.

Zhang, J., Z. Jiang, X. Jiang, S. Wang, C. Liang, and M. Wu, 2016a, Oil generation induces sparry calcite formation in lacustrine mudrock, Eocene of east China: Marine and Petroleum Geology, v. 71, p. 344–359, doi:10.1016/j.marpetgeo.2016.01.007.

Zhang, J., Z. Jiang, C. Liang, J. Wu, B. Xian, and Q. Li, 2016b, Lacustrine massive mudrock in the Eocene Jiyang Depression, Bohai Bay Basin, China: Nature, origin and significance: Marine and Petroleum Geology, v. 77, p. 1042–1055, doi:10.1016/j.marpetgeo.2016.08.008.

Zhang, J., Z. Jiang, L. Liu, F. Yuan, L. Feng, and C. Li, 2021, Lithofacies and depositional evolution of fine-grained sedimentary rocks in the lower submember of the member 3 of Shahejie Formation in Zhanhua Sag, Bohai Bay Basin [in Chinese with English abstract]: Acta Petrolei Sinica, v. 42, no. 3, p. 293–306.

Zhang, J., Z. Jiang, S. Wang, and X. Kong, 2019b, Phytoplankton as main organism in the Eocene organic-rich turbidites of Jiyang Depression, China: Implication for organic matter accumulation mechanism: Energy Sources, Part A: Recovery, Utilization, and Environmental Effects, doi:10.1080/15567036.2019.1677808.

Zhang, L., Z. Cheng, Z. Li, S. Zhang, J. Li, Q. Liu, R. Zhu, J. Zhang, and Y. Bao, 2019a, Structural features and genesis of microscopic pores in lacustrine shale in an oil window: A case study of the Dongying depression: AAPG Bulletin, v. 103, p. 1889–1924, doi:10.1306/1218181522717084.

Zhang, X., and J. Sha, 2012, Sedimentary laminations in the lacustrine Jianshangou Bed of the Yixian Formation at Sihetun, western Liaoning, China: Cretaceous Research, v. 36, p. 96–105, doi:10.1016/j.cretres.2012.02.010.